



HAL
open science

Infiltration of meteoric water in the South Tibetan Detachment (Mount Everest, Himalaya): When and why?

Aude G ebelin, Micah J. Jessup, Christian Teyssier, Michael A. Cosca, Richard D. Law, Maurice Brunel, Andreas Mulch

► To cite this version:

Aude G ebelin, Micah J. Jessup, Christian Teyssier, Michael A. Cosca, Richard D. Law, et al.. Infiltration of meteoric water in the South Tibetan Detachment (Mount Everest, Himalaya): When and why?. *Tectonics*, 2017, 36, pp.690-713. 10.1002/2016TC004399 . insu-03661351

HAL Id: insu-03661351

<https://insu.hal.science/insu-03661351>

Submitted on 6 May 2022

HAL is a multi-disciplinary open access archive for the deposit and dissemination of scientific research documents, whether they are published or not. The documents may come from teaching and research institutions in France or abroad, or from public or private research centers.

L'archive ouverte pluridisciplinaire **HAL**, est destin ee au d ep ot et  a la diffusion de documents scientifiques de niveau recherche, publi es ou non,  emanant des  tablissements d'enseignement et de recherche franais ou  trangers, des laboratoires publics ou priv es.

Copyright

RESEARCH ARTICLE

10.1002/2016TC004399

Special Section:

An Appraisal of Global Continental Crust: Structure and Evolution

Key Points:

- Low δD meteoric fluids permeated the South Tibetan Detachment footwall in the Mount Everest region during mylonitic deformation
- The South Tibetan Detachment system represents an important orogen-scale structure for fault-controlled hydrothermal activity
- Localized north-south extension characterized the upper Tethyan Himalayan plate during the middle Miocene within a convergent setting

Supporting Information:

- Supporting Information S1

Correspondence to:

A. Gébelin,
aude.gebelin@plymouth.ac.uk

Citation:

Gébelin, A., M. J. Jessup, C. Teysier, M. A. Cosca, R. D. Law, M. Brunel, and A. Mulch (2017), Infiltration of meteoric water in the South Tibetan Detachment (Mount Everest, Himalaya): When and why?, *Tectonics*, 36, 690–713, doi:10.1002/2016TC004399.

Received 20 OCT 2016

Accepted 13 MAR 2017

Accepted article online 15 MAR 2017

Published online 25 APR 2017

©2017. American Geophysical Union.
All Rights Reserved.

Infiltration of meteoric water in the South Tibetan Detachment (Mount Everest, Himalaya): When and why?

Aude Gébelin¹ , Micah J. Jessup² , Christian Teysier³, Michael A. Cosca⁴, Richard D. Law⁵ , Maurice Brunel⁶, and Andreas Mulch^{7,8} 

¹School of Geography, Earth and Environmental Sciences, Plymouth University, Plymouth, UK, ²Department of Earth and Planetary Sciences, University of Tennessee, Knoxville, Tennessee, USA, ³Earth Sciences, University of Minnesota, Twin Cities, Minneapolis, Minnesota, USA, ⁴Central Mineral and Environmental Resources Science Center, USGS, Denver, Colorado, USA, ⁵Department of Geosciences, Virginia Polytechnic Institute and State University, Blacksburg, Virginia, USA, ⁶Géosciences Montpellier UMR 5243, Université Montpellier 2, Montpellier, France, ⁷Senckenberg Biodiversity and Climate Research Centre (BiK-F), Frankfurt, Germany, ⁸Institut für Geowissenschaften, Goethe Universität Frankfurt, Frankfurt, Germany

Abstract The South Tibetan Detachment (STD) in the Himalayan orogen juxtaposes low-grade Tethyan Himalayan sequence sedimentary rocks over high-grade metamorphic rocks of the Himalayan crystalline core. We document infiltration of meteoric fluids into the STD footwall at ~17–15 Ma, when recrystallized hydrous minerals equilibrated with low- δD (meteoric) water. Synkinematic biotite collected over 200 m of structural section in the STD mylonitic footwall (Rongbuk Valley, near Mount Everest) record high-temperature isotopic exchange with D-depleted water ($\delta D_{\text{water}} = -150 \pm 5\text{‰}$) that infiltrated the ductile segment of the detachment most likely during mylonitic deformation, although later isotopic exchange cannot be definitively excluded. These minerals also reveal a uniform pattern of middle Miocene (15 Ma) ⁴⁰Ar/³⁹Ar plateau ages. The presence of low- δD meteoric water in the STD mylonitic footwall is further supported by hornblende and chlorite with very low δD values of -183‰ and -162‰ , respectively. The δD values in the STD footwall suggest that surface-derived fluids were channeled down to the brittle-ductile transition. Migration of fluids from the Earth's surface to the active mylonitic detachment footwall may have been achieved by fluid flow along steep normal faults that developed during synconvergent extension of the upper Tethyan Himalayan plate. High heat flow helped sustain buoyancy-driven fluid convection over the timescale of detachment tectonics. Low δD values in synkinematic fluids are indicative of precipitation-derived fluids sourced at high elevation and document that the ground surface above this section of the STD had already attained similar-to-modern topographic elevations in the middle Miocene.

1. Introduction

Assessing the role of fluids in detachment systems is important because fluids may influence the mechanisms and rates of detachment faulting from the grain scale to the scale of entire faults/shear zones [e.g., Mulch *et al.*, 2006; Whitney *et al.*, 2013]. Fluid infiltration along and within shear zones can induce metamorphic reactions [e.g., Mertanen and Karell, 2012; Saxena *et al.*, 2012] and influence deformation mechanisms (recrystallization and recovery) by formation of rheologically weak phyllosilicate layers that may localize deformation [Wintsch *et al.*, 1995; Warr and Cox, 2001] or by enhancing crystal-scale recrystallization [Rutter and Mainprice, 1979; Paterson, 1995]. The presence of phyllosilicates may favor intergranular pressure solution processes [Renard *et al.*, 2001] and thus reduce the porosity and permeability of deforming rocks. Combined recrystallization and fluid-mediated element transport are hence critical in controlling the porosity and permeability structure of deforming crystalline rocks [Person *et al.*, 2007].

Infiltration of meteoric fluids has been documented in the footwall of detachment zones that bound the metamorphic core complexes of the North American Cordillera, based mainly on the low hydrogen (δD) and oxygen ($\delta^{18}O$) isotope values of synkinematic hydrous minerals [e.g., Fricke *et al.*, 1992; Losh, 1997; Mulch *et al.*, 2004, 2006; Holk and Taylor, 2007; Gottardi *et al.*, 2011; Gébelin *et al.*, 2011, 2012, 2015; Methner *et al.*, 2015; Quilichini *et al.*, 2015, 2016], the Menderes Massif of Turkey [Hetzl *et al.*, 2013], and extensional detachments in the European Central Alps [Campani *et al.*, 2012]. Surface fluids penetrated the deforming crust down to the brittle-ductile transition in these orogens by means of normal faults and fractures that

dissected the brittle upper crust, while at the same time movement within the detachment zone induced advection of hot footwall material that promoted buoyancy-driven fluid convection [e.g., *Person et al.*, 2007]. The downward migration of fluids is also facilitated by the presence of a hydraulic head that is generated in high-relief areas such as domino-style tilted blocks of upper crust [*Person et al.*, 2007]. Therefore, detachment zones represent a domain in the crust where surface fluids and metamorphic fluids may meet [e.g., *Fricke et al.*, 1992; *Nesbitt and Muehlenbachs*, 1995; *Losh*, 1997; *Mulch et al.*, 2004, 2006; *Holk and Taylor*, 2007; *Gébelin et al.*, 2011, 2015].

Here we document similar fluid infiltration into the South Tibetan Detachment (STD) of the Himalayan orogen that may be viewed as a special category of normal-sense shear detachments because it developed during overall continental convergence. Some authors consider it as a passive structure [e.g., *Chemenda et al.*, 2000; *Ring and Glodny*, 2010] that formed to accommodate the exhumation of underlying rocks in an extruded wedge or a flowing channel [e.g., *Burg et al.*, 1984; *Burchfiel and Royden*, 1985; *Grujic et al.*, 1996, 2002; *Grasemann et al.*, 1999; *Beaumont et al.*, 2001, 2004; *Searle et al.*, 2003; *Godin et al.*, 2006]. Others view the STD as a thrust that was reactivated as a top-to-the-north shear zone and alternatively played the role of passive-roof and active-roof thrust during emplacement of the Himalayan crystalline core (HCC) [e.g., *Yin*, 2006; *Webb et al.*, 2011]. Here we show that at least from a crustal permeability standpoint the STD is similar to extensional detachments of the metamorphic core complexes of western North America. We suggest that localized hydration of the STD footwall was enhanced by the combined effects of porosity and permeability pathways in the overlying Tethyan sedimentary rocks and high heat flow in the metamorphic footwall.

To determine fluid provenance and the timing and duration of fluid flow in the STD footwall, we use a combination of hydrogen isotope (δD) geochemistry and $^{40}\text{Ar}/^{39}\text{Ar}$ geochronology of hydrous minerals from STD mylonites collected in the Rongbuk Valley, located to the north of Mount Everest. This analytical approach, pioneered in the North American Cordillera [e.g., *Fricke et al.*, 1992; *Losh*, 1997; *Mulch et al.*, 2004], is based on the concept of water-rock interaction in active crustal-scale shear zones and involves measurement of δD values of hydrous minerals (e.g., mica and amphibole) that interacted with aqueous fluids at high temperature. If mineral water-hydrogen isotope equilibrium was achieved during deformation and recrystallization, and if the temperature of hydrogen isotope exchange can be independently estimated, δD values of fluids can be retrieved from synkinematic minerals through experimentally calibrated hydrogen isotope exchange parameters.

The δD values of hydrous minerals have been recognized to be sensitive tracers of fluid-rock interaction because hydrogen is a constituent of the H_2O molecule itself and is a trace element in silicate rocks (order of 2000 ppm; e.g., *Sheppard* [1986]) compared to oxygen, which is typically the most abundant element in rocks. Therefore, a small amount of fluid will be detectable by measuring the hydrogen isotope ratios because the volume of fluid required for changing the hydrogen bulk-rock composition of a unit is several orders of magnitude smaller than that required for changing the oxygen bulk-rock composition. Hydrogen also provides a wide range of δD values in silicates [*Coplen et al.*, 2002] that allow the origin of fluids involved in the formation or alteration of hydrogen-bearing silicates to be determined (e.g., $\delta D_{\text{sea water}} = 0 \pm 1\text{--}2\text{‰}$, *Hoefs* [2004]; $-80\text{‰} < \delta D_{\text{magmatic fluids}} < -40\text{‰}$, e.g., *Sheppard* [1986]; $-70\text{‰} < \delta D_{\text{metamorphic fluids}} < -20\text{‰}$, e.g., *Field and Fifarek* [1985]; $-495\text{‰} < \delta D_{\text{meteoric water}} < +129\text{‰}$, e.g., *Fontes and Gonfiantini* [1967] and *Jouzel et al.* [1987]).

Negative δD values for hydrous silicates ($< -120\text{‰}$) are a valuable indicator of interaction with meteoric fluids [e.g., *Taylor*, 1990; *Mulch et al.*, 2004, 2006; *Gébelin et al.*, 2011, 2012, 2015] because δD values in precipitation decrease with increasing altitude on the windward side of mountain ranges ($\sim 20\text{‰}$ in δD per kilometer; e.g., *Poage and Chamberlain* [2001]) and low- δD fluids are typically absent in the crust. The presence of cool surface-derived fluids descending into the brittle-ductile transition influences the thermomechanical behavior of shear zones and also impacts the radiogenic isotope chronometers at this critical structural level within the continental crust [e.g., *Mulch et al.*, 2005; *Gottardi et al.*, 2011]. Therefore, combining hydrogen isotope and $^{40}\text{Ar}/^{39}\text{Ar}$ geochronology data from a transect across the STD into the underlying mylonitic footwall provides insight on the origin of fluids within the shear zone exposed in the northern part of the Rongbuk Valley, as well as the timing and possible duration of fluid flow and isotope exchange (hydrogen and argon) between mineral grains and circulating fluids.

The Rongbuk Valley mylonites (Figure 1) provide an excellent target for assessing the role of fluids in the STD because (1) the structural, metamorphic, and geochronologic record of the region is well established [e.g., Burchfiel *et al.*, 1992; Hodges *et al.*, 1992, 1998; Carosi *et al.*, 1998; Searle *et al.*, 2003, 2006; Law *et al.*, 2004, 2011; Jessup *et al.*, 2006, 2008; Cottle *et al.*, 2015; Schultz *et al.*, 2017]; (2) the region had a high geothermal gradient in part generated by the emplacement of syntectonic leucogranite bodies in the STD footwall [Hodges *et al.*, 1998; Murphy and Harrison, 1999; Searle *et al.*, 2003]; and (3) surface topography and relief were sufficiently high during motion on the STD to create a regional hydraulic head [Gébelin *et al.*, 2013].

The new data presented here support previous claims that surface-derived fluids infiltrated the detachment shear zone over a minimum duration of circa 2 Myr in response to localized extension associated with development of steep normal faults in Tethyan Himalayan sequence hanging wall rocks at ~17–15 Ma.

2. Tectonic Setting

2.1. Tectonic Architecture of the Himalaya

For more than 1500 km along strike the STD parallels the east-west arcuate trend of the Himalayan range and juxtaposes unmetamorphosed or low-grade Tethyan Himalayan sequence (THS) sedimentary rocks over high-grade metamorphic rocks of the HCC (Figure 1a; e.g., Burg *et al.* [1984] and Burchfiel *et al.* [1992]). The ~25 km thick HCC slab of metasedimentary and granitic rocks is bounded along the base by the south directed Main Central Thrust (MCT) that separates the HCC from lower grade Lesser Himalayan sequence (LHS) rocks [e.g., Heim and Gansser, 1939; LeFort, 1975; Pêcher, 1989; Searle *et al.*, 2008]. Structural and geochronological studies indicate that activity on the MCT and the STD was spatially and temporally related and played a major role in exhuming the HCC all along the Himalayan range [e.g., Burchfiel and Royden, 1985; Grujic *et al.*, 1996, 2002; Beaumont *et al.*, 2004; Webb *et al.*, 2011] between 24 and 12 Ma [e.g., Hodges *et al.*, 1992, 1996; Murphy and Harrison, 1999; Vannay and Grasemann, 2001; Daniel *et al.*, 2003; Searle *et al.*, 2003; Godin *et al.*, 2006; Kellett *et al.*, 2009, 2010; Leloup *et al.*, 2010; Chambers *et al.*, 2011; Kellett and Grujic, 2012].

Various models have been proposed to explain emplacement of the HCC. In the channel flow model [e.g., Nelson *et al.*, 1996; Hodges *et al.*, 2001; Beaumont *et al.*, 2001, 2004], the MCT and STD are viewed as parallel structures that channelize the southward extrusion of partially molten crust sustained by continued erosion at the Himalayan front. In the wedge extrusion model [e.g., Burg *et al.*, 1984; Burchfiel and Royden, 1985; Grujic *et al.*, 1996], the MCT and STD merge downdip and facilitate exhumation of the HCC within the Indian crust as a wedge. Grujic *et al.* [2011] proposed a hybrid model of the channel flow and wedge models. The tectonic wedging model is radically different from the other models; in this model the HCC is bounded by the MCT and STD surfaces that merge in their updip direction [e.g., Yin, 2006; Webb *et al.*, 2007, 2011]. Although these models have differences in timing and style, all attempt to explain Miocene exhumation of the HCC. In the channel flow and wedge extrusion models, southward crustal flow is enhanced by both erosion at the Himalayan front and north directed normal-sense slip on the STD that facilitates southward movement of low-viscosity material, whereas in the tectonic wedging model, exhumation of the HCC is a consequence of crustal thickening by accretion and interleaving of thrust slices. The resolution of this debate relies in part on the tectonic regime that prevailed in the overlying Tethyan Himalayan sequence and on the timing, kinematics, and magnitude of motion on the STD.

2.2. Metamorphic History of the Mount Everest Region

Prior to localization of deformation along the STD in the Everest region, the HCC (including the Everest series) was buried during crustal thickening that resulted in Barrovian metamorphism at ~650°C, 6 kbar [Pognante and Benna, 1993; Carosi *et al.*, 1998; Searle *et al.*, 2003; Jessup *et al.*, 2008] at around ~32 Ma in the upper reaches of the Khumbu region [Simpson *et al.*, 2000; Searle *et al.*, 2003]. At similar structural positions exposed in the Kangshung Valley on the east side of Everest, U-Th-Pb dating indicates that peak-Barrovian conditions were reached by at least ~38.9 Ma [Cottle *et al.*, 2009]. This was followed by sillimanite-grade metamorphism at ~28 Ma [Cottle *et al.*, 2009]. In structurally higher positions within the northward dipping HCC, exposed to the north of the Kangshung Valley, the regional metamorphism occurred later at ~25.4 Ma [Cottle *et al.*, 2009].

In the upper portions of the HCC, as exposed in the Khumbu region, the record of Barrovian metamorphism was variably overprinted by isothermal, high temperature (>620°C) and moderate pressure (~3–5 kbar) metamorphism associated with Miocene partial melting and decompression [Pognante and Benna, 1993;

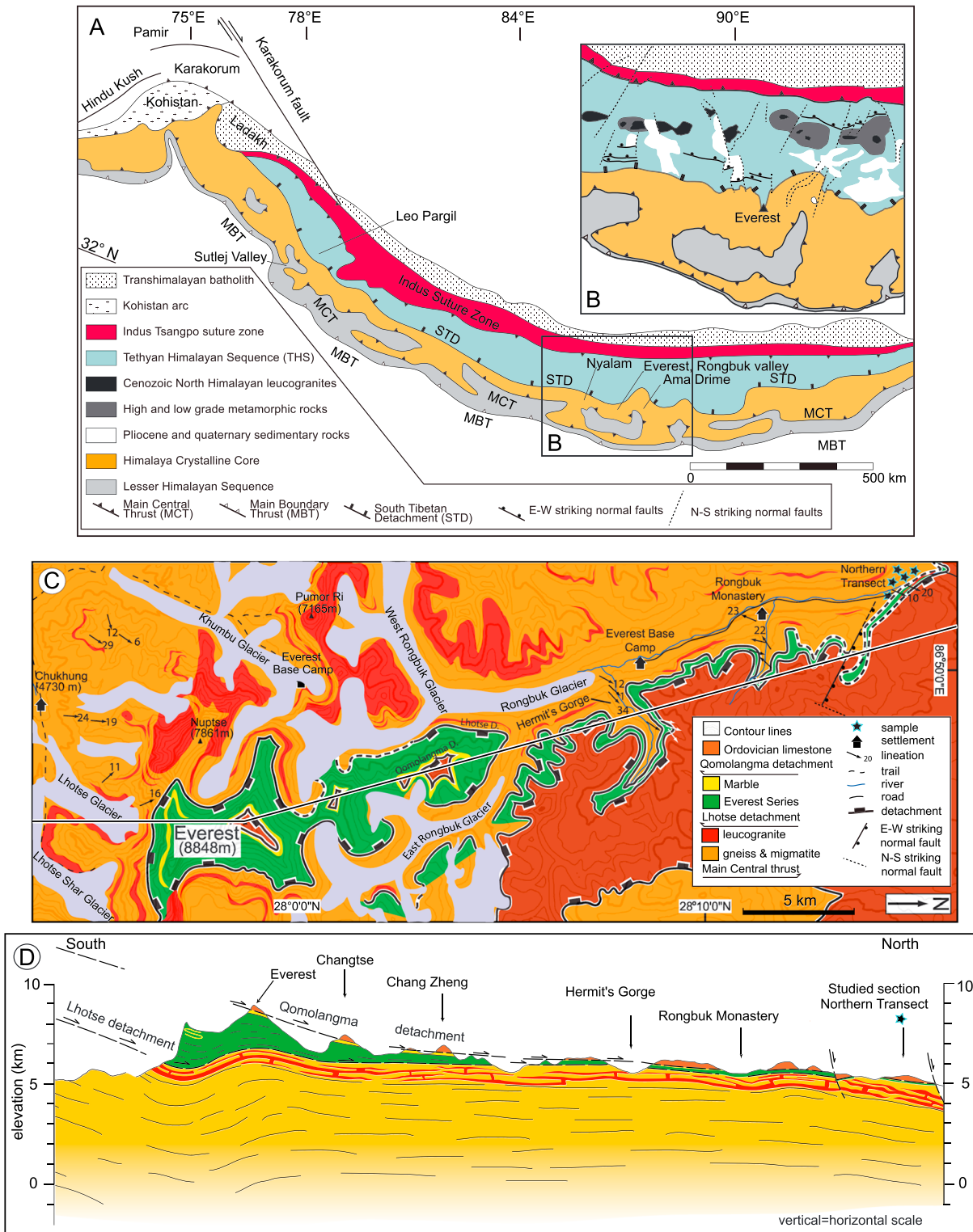


Figure 1. (a) Simplified geologic sketch map of the Himalaya showing distribution of the main lithotectonic units and main areas discussed in text (modified after Burchfiel *et al.* [1992] and Searle *et al.* [2008]). (b) Tectonic map of the Mount Everest region modified after Burchfiel *et al.* [1992]. (c) Simplified geological map of the Mount Everest region and Rongbuk Valley, Tibet (modified after Chi-Hsiang and Shih-Tseng [1978], Carosi *et al.* [1998], Searle [2003], and Jessup *et al.* [2006, 2008]). (d) N-S cross section across Mount Everest (modified after Searle [2003] and Jessup *et al.* [2006, 2008]) showing the upper brittle Qomolangma detachment and the lower ductile Lhotse detachment merging toward the north into the South Tibetan Detachment shear zone; position of studied section is indicated.

Carosi *et al.*, 1998; Searle *et al.*, 2003; Jessup *et al.*, 2008]. High temperatures characterized the Khumbu area rocks between ~32 and 17 Ma [Searle *et al.*, 2010], induced partial melting between ~26 and 20 Ma [Viskupic *et al.*, 2005], and fed the overlying leucogranite injection complexes [Carosi *et al.*, 1999; Searle *et al.*, 2003]. Similar structural positions in the Kangshung Valley also record partial melting at ~20.8 Ma (prekinematic to synkinematic) and 16.7 Ma (postkinematic) [Cottle *et al.*, 2009]. Early metamorphism at higher structural positions within the northward dipping HCC was overprinted by a metamorphic event at ~16.1 Ma that was followed by partial melting at ~15.2 Ma (prekinematic to synkinematic) and ~12.6 Ma (postkinematic; Cottle *et al.* [2009]). When combined with data from a north Himalayan gneiss dome, Cottle *et al.* [2009] proposed that the HCC recorded metamorphism and partial melting that resulted in flow of a weakened, southward directed channel for 20 Myr. prior to ~16 Ma.

2.3. Timing of Deformation in the Mount Everest Region

The timing of STD activity varies significantly along the Himalayan belt covering the early to middle Miocene [Hodges *et al.*, 1992; Godin *et al.*, 2006; Carosi *et al.*, 2013], an age range that mimics ages obtained for activity on the MCT.

In the structurally highest position of the HCC near Mount Everest (Hermit's Gorge of Rongbuk Valley) (Figures 1c and 1d), various generations of leucogranite record a minimum age of ~16.4 Ma for ductile fabric development related to deformation along the STD, while extrusion of partially melted sillimanite-grade rocks beneath a passive-roof fault occurred prior to 15.4 Ma [Cottle *et al.*, 2015]. In the same area, U-Pb ages from sheared schist (16.9 ± 2 Ma) were interpreted as evidence for movement on the STD at this time [Searle *et al.*, 2003].

Farther to the north in Rongbuk Valley, a series of leucogranite dikes and sills exposed in the cliffs above Rongbuk Monastery (Figures 1c and 1d) record the timing of ductile deformation at ~17 Ma [Murphy and Harrison, 1999]. The northernmost dated mylonitic leucogranite sill (100–150 m thick) recorded an upper bound for the timing of the shear zone of 16.67 ± 0.04 Ma (U/Pb; Hodges *et al.* [1998]).

Despite some lack of precision, the cessation of movement on the STD occurred during the middle to late Miocene [e.g., Edwards *et al.*, 1996, 1999; Wu *et al.*, 1998; Kellett *et al.*, 2009, 2013; Schultz *et al.*, 2017]. However, based on field relations combined with monazite U-Pb data from leucogranite dikes at Hermit's Gorge, Cottle *et al.* [2015] proposed a minimum age of 15.6 Ma for ductile shearing on the STD. The end of shearing on the STD footwall must reflect important geodynamic changes in the south Tibetan region. It is marked by a transition at ~15–13 Ma [Nagy *et al.*, 2015] from N-S stretching and south directed extrusion of the HCC, as evidenced by E-W striking extensional shear zones and normal faults (Figure 1b; Chi-Hsiang and Shih-Tseng [1978], Burchfiel *et al.* [1992], and Carosi *et al.* [1998]), to orogen-parallel E-W stretching/extension accommodated by the development of high-angle N-S striking normal faults that formed perpendicular to the gently dipping STD along the length of the Himalayan orogen [e.g., Jessup and Cottle, 2010; Leloup *et al.*, 2010; Lee *et al.*, 2011; Nagy *et al.*, 2015].

Hydrogen isotope ratios (δD) in silicate minerals that crystallized in the immediate footwall to the STD exposed in the Rongbuk Valley indicate that meteoric water penetrated the ductile segment of the detachment over the timescale of mylonitic deformation [Gébelin *et al.*, 2013]. Based on geochronological data from syntectonic leucogranite and sheared biotite-schist (see above, Hodges *et al.* [1998], Murphy and Harrison [1999], and Searle *et al.* [2003]) hydrogen isotope exchange between meteoric fluids and recrystallized silicates is thought to have occurred at ~17 Ma during normal-sense movement on the STD [Gébelin *et al.*, 2013]. In addition to the δD values of biotite and hornblende presented in Gébelin *et al.* [2013], the present study offers a more complete set of hydrogen isotope data and microstructural observations, as well as new $^{40}\text{Ar}/^{39}\text{Ar}$ geochronological data from the STD footwall in the Rongbuk Valley indicating that fluid-rock isotopic exchange occurred over a longer time interval and ceased shortly before 15 Ma.

The presence of low- δD meteoric water in the STD footwall raises the question of how these fluids reached down to the brittle-ductile transition. Although a wide range of structural and thermochronological data for the STD have been recorded along the length of the Himalaya, the relationship between the timing of deformation, fluid flow, and normal-sense northward shearing along the STD remains elusive. The results presented here shed new light on Miocene crustal hydrology in the Himalaya region and offer new ideas regarding the relationship among crustal deformation, Himalayan topography, and fluid circulation along the STD.

3. Rongbuk Valley Transect: Petrography and Deformation Temperatures

We collected oriented samples for structural analysis along a transect from the STD into the underlying mylonitic footwall in the Rongbuk Valley immediately north of Mount Everest (Figures 1b and 1c). In this area, the STD consists of two major detachment zones that gradually merge northward (Figure 1d): the brittle Qomolangma detachment (QD) and the structurally lower ductile Lhotse detachment shear zone (LD) [Burchfiel *et al.*, 1992; Carosi *et al.*, 1998; Searle, 2003; Searle *et al.*, 2003; Sakai *et al.*, 2005].

The QD represents a sharp zone that juxtaposes low-grade Ordovician limestone [Corthouts *et al.*, 2015, and references therein] against underlying coarse-grained recrystallized marbles of the Yellow Band (Figures 1c and 1d). The sheared marbles below the QD form the top of the Everest Series and are underlain by metapelites in which metamorphic grade increases downward from greenschist to lower amphibolite facies in the structural section [Pognante and Benna, 1993; Lombardo *et al.*, 1993; Waters *et al.*, 2006; Jessup *et al.*, 2008]. The LD separates these penetratively deformed metasedimentary rocks from underlying biotite-schists and gneisses (sillimanite grade) injected by leucogranite sills [Searle, 2003; Searle *et al.*, 2003] that form the upper part of the Himalayan crystalline core.

Our samples were collected from the Northern Transect [Jessup *et al.*, 2006; Law *et al.*, 2011] located at the northern end of Rongbuk Valley, ~35 km to the north of Mount Everest (Figures 1c and 1d). Here the QD and LD merge and form a single high-strain detachment zone that separates upper plate Tethyan limestone from high-grade metamorphic rocks and syntectonic leucogranite below (Figure 1d). Quartz-rich layers at the top of the detachment footwall display intense dynamic recrystallization with development of subgrains and window microstructures or isolated grains (i.e., “leftover grains” of Jessel [1987]) indicating that subgrain rotation and grain boundary migration were the dominant dynamic recrystallization processes [Hirth and Tullis, 1992; Jessup *et al.*, 2006]. This deformation mechanism can occur over a wide temperature range (400°C to $\geq 550^\circ\text{C}$) as indicated by the opening angle of quartz *c* axes fabrics in samples from the Northern Transect that are systematically consistent with deformation temperatures of $\geq 540^\circ\text{C}$ (Figure 3; Law *et al.* [2011], Law [2014], and Faleiros *et al.* [2016]).

Mylonitic leucogranite sills intruding marbles within the top 7 m of the section contain abundant muscovite (>30%) forming elongate lenticular mica fish and fish with small aspect ratios and curved tails [Ten Grotenhuis *et al.*, 2003] that are consistent with top-to-northeast sense of shear (Figures 2a and 3). In contrast, mica fish observed in mylonitic cross-cutting leucogranites in deeper parts (≥ 31 m) of the section have sigmoidal cleavage planes that converge at both tips of the mica grain (Figures 2b and 3; Ten Grotenhuis *et al.* [2003]).

Calc-silicate units in the immediate footwall to the detachment exposed on the Northern Transect contain abundant quartz and feldspar grains, as well as amphibole and biotite grains oriented subparallel to foliation (Figure 2c). Tension gashes oriented perpendicular to the NNE-SSW trending stretching lineation are filled by chlorite [Jessup *et al.*, 2006] and postdate the main foliation (Figure 2d). The calc-silicate units are underlain by biotite-schists and gneisses that represent the structurally lowest unit exposed on the Northern Transect. Biotite is abundant and forms shear bands consistent with top-to-north sense of shear (Figures 2e and 2f). Biotite grains are locally kinked, indicating late-stage deformation under low-grade conditions.

4. Hydrogen Isotope Geochemistry

The δD values of biotite, hornblende, muscovite, and chlorite were measured in 23 samples of sheared leucogranite, pegmatite, biotite-schist/gneiss, and calc-silicate across approximately 200 m of structural section from the STD into the underlying mylonitic footwall (Figure 3 and Table 1); analytical procedures are summarized in the supporting information (Text 1). These samples include δD values for biotite and hornblende previously reported by Gébelin *et al.* [2013] (see their Table DR1 in Data Repository). As the presence of fluid during mylonitization can induce the breakdown of porphyroclasts and the growth of newly recrystallized grains [e.g., Paterson, 1995; Gébelin *et al.*, 2011; Quilichini *et al.*, 2015], different grain size fractions were measured in order to identify potentially different generations of hydrous minerals.

4.1. Hydrogen Isotope Composition of Minerals From Biotite-Schist and Calc-Silicate Samples

Biotite from the biotite-schist and calc-silicate rock samples analyzed is characterized by very low δD values of -132‰ to -176‰ at distances of 9–109 m beneath the STD and attains progressively higher values of up to

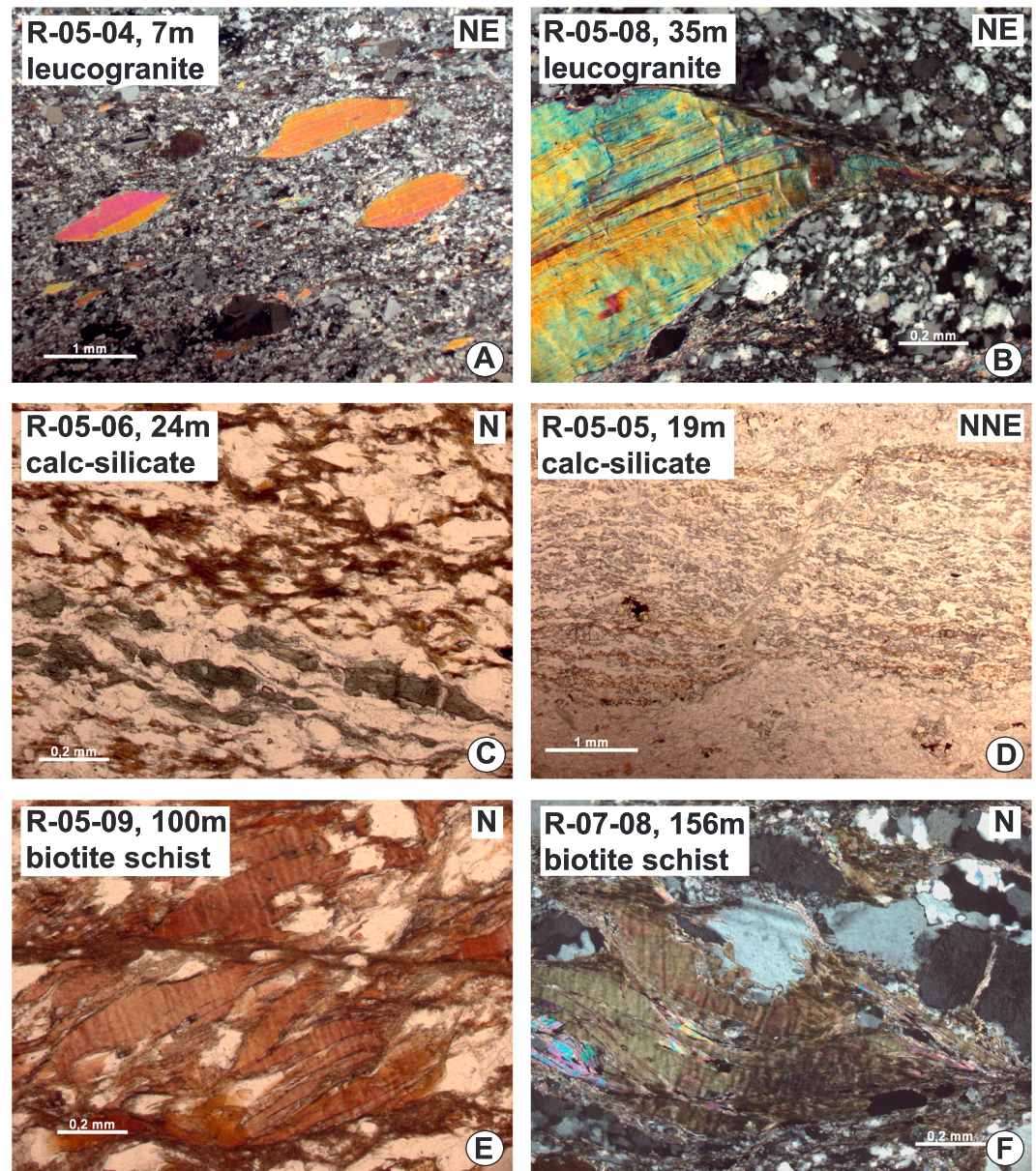


Figure 2. Photomicrograph of mylonitic rocks collected in the footwall to the STD exposed on the Northern Transect, Rongbuk Valley (sample number, lithology, and sampling depth beneath the detachment are indicated). All thin sections cut perpendicular to foliation and parallel to mineral lineation. (a) Muscovite fish with small aspect ratios [Ten Grotenhuis *et al.*, 2003] indicating top-to-northeast sense of shear. (b) Muscovite fish showing sigmoidal cleavage planes converging at the tip of the grain [Ten Grotenhuis *et al.*, 2003] consistent with a top-to-northeast normal sense of shear. (c) Elongated amphibole and biotite grains parallel to the foliation in calc-silicate. (d) Microboudinage and tension gashes filled by chlorite in calc-silicate postdating the main foliation. (e) Biotite-bearing shear bands indicating top-to-north sense of shear. (f) Biotite fish from schist.

–85‰ (156 m) toward the base of the section. Similarly, hornblende separates from two calc-silicate samples at 24 and 98 m beneath the detachment yield very low δD values of –183 and –181‰, respectively. Chlorite from one calc-silicate sample has a very low δD value of –162‰.

4.2. Hydrogen Isotope Composition of Minerals From Leucogranite Samples

Syntectonic leucogranites at 25–97 m beneath the detachment contain biotite grains characterized by low δD values that range from –126‰ to –182‰. Muscovite grains from the leucogranites have higher δD values (between –129 and –77‰) than biotite grains, even though they are from similar, and in some

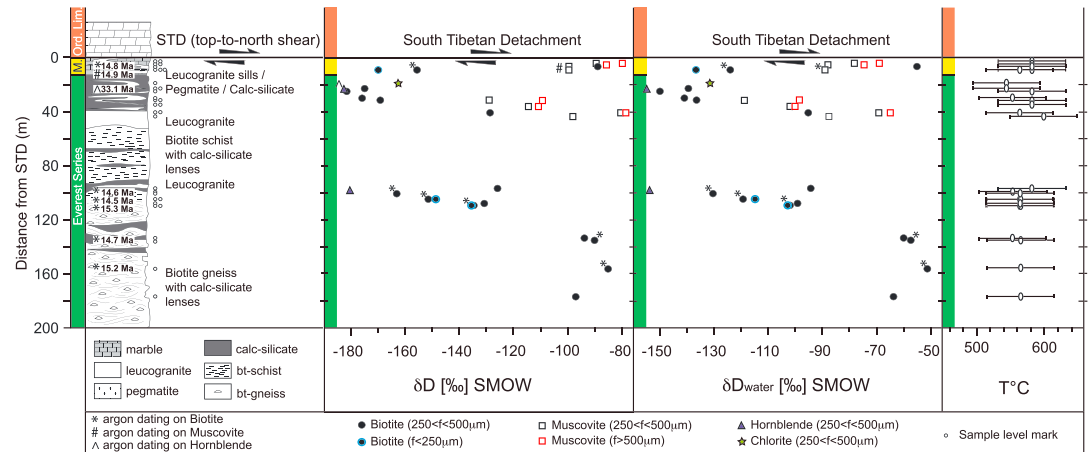


Figure 3. The δD values of biotite, muscovite, hornblende, and chlorite from mylonitic rocks in the footwall of the South Tibetan Detachment (STD) and calculated δD_{water} values. Most of sample separates are from the grain size fraction $250 < f < 500 \mu\text{m}$, except those shown in red ($f > 500 \mu\text{m}$) and blue ($f < 250 \mu\text{m}$). Note that the δD values of biotite and hornblende are those previously published in *Gébelin et al.* [2013]. (left) Lithologic section through the STD at Northern Transect (Rongbuk Valley). Note that $^{40}\text{Ar}/^{39}\text{Ar}$ results are given with respect to their structural position on the stratigraphic column. (right) Deformation/recrystallization temperatures based on opening angle of quartz c axes fabric patterns with nominal uncertainties of $\pm 50^\circ\text{C}$ [Law et al., 2011].

cases the same, leucogranite samples collected at distances less than 41 m beneath the detachment. The highest δD values for muscovite grains (-77 to -86‰) from leucogranite samples fall within the δD range of metamorphic muscovite [e.g., *Sheppard*, 1986] and occur within the 0–7 m and 40 m depth intervals. In addition, we note that the largest muscovite size fractions ($f > 500 \mu\text{m}$) yield δD values up to 20‰ higher than the smallest size fractions ($250 < f < 500 \mu\text{m}$) (Table 1).

5. $^{40}\text{Ar}/^{39}\text{Ar}$ Geochronology

We dated seven samples of schist, leucogranite, and calc-silicate collected over 156 m of section of STD footwall mylonites (Figure 4 and Table 2). In an attempt to make a link between potential hydrogen isotope and ^{40}Ar loss, we selected samples from which we had previously obtained low δD values at the top of the section and high δD values at the bottom of the section. Analyses were conducted on multigrain mineral separates using furnace step-heating $^{40}\text{Ar}/^{39}\text{Ar}$ geochronology (Table 2; analytical procedures can be found in Text 2 of the supporting information; *Dalrymple et al.* [1981], *Min et al.* [2000], *Lee et al.* [2006], and *Kuiper et al.* [2008]). Plateau ages of biotite fish from samples M2 (9 m below detachment), R-05-09 (100 m), R-07-03 (104 m), R-07-05 (109 m), R-07-07 (134 m), and R-07-08 (156 m) are 14.77 ± 0.17 Ma, 14.61 ± 0.13 Ma, 14.54 ± 0.11 Ma, 15.25 ± 0.13 Ma, 14.72 ± 0.11 Ma, and 15.16 ± 0.15 Ma, respectively (Figure 4). A multigrain muscovite separate from sample M2 yields a plateau age of 14.89 ± 0.07 Ma. These muscovite grains are from a syntectonic leucogranite sill that parallels the foliation in biotite-schist sample M2.

In contrast, hornblende separates from calc-silicates (sample R-05-06; 24 m below detachment) provide a disturbed $^{40}\text{Ar}/^{39}\text{Ar}$ age spectrum with low-temperature release steps indicating Eocene ages, followed by a plateau-like spectrum defined by two higher-temperature release steps that include $\sim 79\%$ of ^{39}Ar and give a late Eocene-early Oligocene age of 33.0 ± 0.8 Ma (Figure 4). The last step that comprises $\sim 10\%$ of total ^{39}Ar released gives an early to middle Miocene age.

6. Discussion

Two lines of evidence point to operation of the STD in the Mount Everest region as a hydrothermal system that permitted the circulation of meteoric water during a restricted time interval in the middle Miocene:

1. $\delta D_{\text{biotite}}$ values as low as -182‰ require the presence of meteoric fluids in the detachment footwall during deformation [e.g., *Taylor*, 1990]. Infiltration of surface-derived fluids down to the brittle-ductile transition is also supported by low $\delta D_{\text{hornblende}}$ and $\delta D_{\text{chlorite}}$ values of -182‰ and -162‰ , respectively. Consistent with localized meteoric fluid flow in the topmost part of the detachment footwall, δD values

Table 1. Hydrogen Isotope Compositions of Biotite, Muscovite, Hornblende, and Chlorite and Temperature of Deformation/Recrystallization ($\pm 50^\circ\text{C}$) for Mylonitic Rocks From the Footwall to the STD Exposed in the Northern Transect, Rongbuk Valley^a

Sample	Distance Beneath STD (m)	Rock Type	δDBt (‰)	δDMs (‰)	δDHbl (‰)	δDChl (‰)	Grain Size Fraction (μm)	$T^\circ\text{C}$ Recrystallization	$\delta\text{D}_{\text{water}}$ From Bt (‰)	$\delta\text{D}_{\text{water}}$ From Ms (‰)	$\delta\text{D}_{\text{water}}$ From Hbl (‰)	$\delta\text{D}_{\text{water}}$ From Chl (‰)
R-05-03	-6	leucogranite	-89	-89			250 < f < 500	581		-78		
R-05-03	-6	leucogranite	-80	-80			f > 500	581		-69		
R-05-04	-7	leucogranite	-100	-100			250 < f < 500	581		-89		
R-05-04	-7	leucogranite	-86	-86			f > 500	581		-75		
M1	-8	leucogranite	-88	-88			250 < f < 500	581	-56			
M2	-9	schist/pegmatite	-156	-100			250 < f < 500	581	-124	-89		
M3	-9	bt-schist	-170				100 < f < 180	565	-137			
R-05-05	-19	calc-silicate			-162		250 < f < 500	543				-132
R-05-06	-24	calc-silicate	-174	-183			250 < f < 500	543	-139		-155	
R-05-07	-25	leucogranite	-182				250 < f < 500	581	-150			
R-03-23	-30	calc-silicate	-176				250 < f < 500	555	-141			
R-03-24	-31	leucogranite	-169	-129			250 < f < 500	581	-137	-118		
R-03-24	-31	leucogranite	-109	-109			f > 500	581		-98		
R-05-08	-35	leucogranite	-114	-114			250 < f < 500	581		-103		
R-05-08	-35	leucogranite	-111	-111			f > 500	581		-100		
R-03-25	-40	leucogranite	-129	-81			250 < f < 500	565	-96	-69		
R-03-26	-41	leucogranite	-77	-77			f > 500	565		-65		
R-07-01	-97	leucogranite	-126	-98			250 < f < 500	599		-88		
R-07-02	-98	calc-silicate			-181		250 < f < 500	581	-94		-154	
R-05-09	-100	bt-schist	-163				250 < f < 500	555				
R-07-03	-104	bt-schist	-152				250 < f < 500	565	-130			
R-07-03	-104	bt-schist	-148				250 < f < 500	565	-119			
R-07-04	-107	bt-schist	-132				180 < f < 250	565	-115			
R-07-05	-109	bt-schist	-135				250 < f < 500	565	-99			
R-07-05	-109	bt-schist	-135				250 < f < 500	565	-102			
R-07-06	-132	calc-silicate	-94				180 < f < 250	565	-102			
R-07-07	-134	bt gneiss	-90				250 < f < 500	555	-60			
R-07-08	-156	bt gneiss	-85				250 < f < 500	565	-57			
R-07-09	-177	bt gneiss	-97				250 < f < 500	565	-52			
R-07-09	-177	bt gneiss	-97				250 < f < 500	565	-64			

^aNote that calculated associated $\delta\text{D}_{\text{water}}$ values are also mentioned.

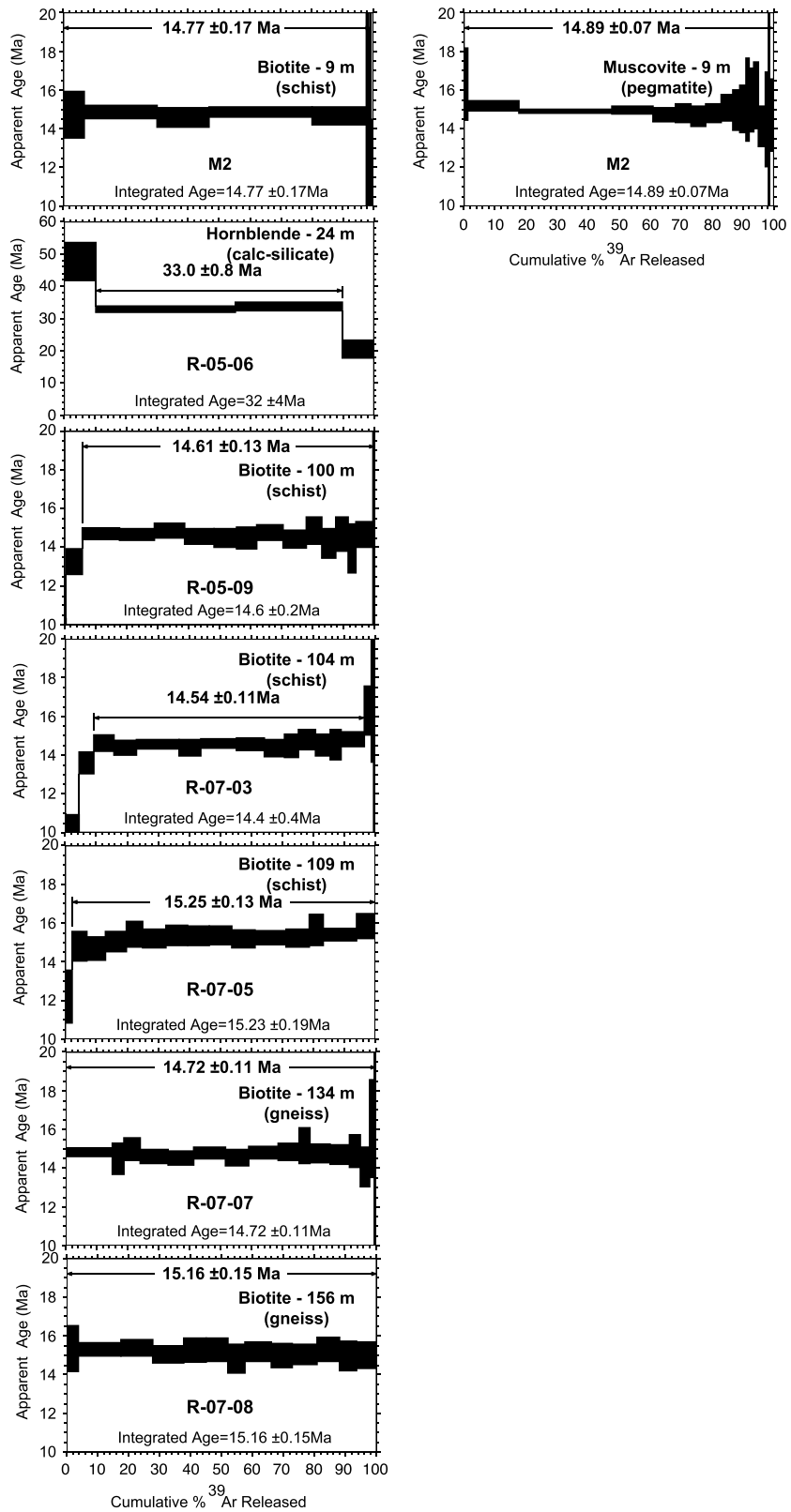


Figure 4. The $^{40}\text{Ar}/^{39}\text{Ar}$ Ar step-heating spectra of biotite, muscovite, and hornblende from mylonitic rocks from the STD at Northern Transect, Rongbuk Valley.

Table 2. Furnace Step-Heating $^{40}\text{Ar}/^{39}\text{Ar}$ Data For biotite, Muscovite, and Hornblende From Mylonitic Rocks From the Footwall to the STD Exposed in the Northern Transect, Rongbuk Valley^a

Lab Run ID	CO ₂ Laser Power (W)	Measured Signals ($\times 10^{-15}\text{A}$)					Derived Results													
		^{40}Ar $\pm 1\sigma$	^{39}Ar $\pm 1\sigma$	^{38}Ar $\pm 1\sigma$	^{37}Ar $\pm 1\sigma$	^{36}Ar $\pm 1\sigma$	^{39}Ar Mol % of Total $^{10-14}$	Ca/K $\pm 1\sigma$	$^{40}\text{Ar}/^{39}\text{Ar}$ $\pm 1\sigma$	% ⁴⁰ Ar*	Age (Ma) $\pm 1\sigma$									
M2, muscovite^b; $J \pm 1\sigma = 0.001071 \pm 0.000002$; 9 m beneath the STD																				
935-01C	0.80	304.754	1.121	6.2545	0.2830	-0.0452	0.1555	-0.0510	0.1219	0.8458	0.0048	0.0191	1.50	-0.07	0.18	8.34	0.48	17.13	16.28	0.92
935-01D	0.90	1509.292	1.179	68.1272	0.2867	1.5227	0.1549	0.0154	0.1240	3.2836	0.0135	0.2078	16.31	0.00	0.02	7.76	0.07	35.05	15.15	0.14
935-01E	1.00	1239.975	1.150	125.9781	0.2951	1.8144	0.1541	0.2483	0.1210	0.9377	0.0048	0.3842	30.16	0.02	0.01	7.62	0.02	77.43	14.87	0.04
935-01F	1.10	570.212	1.127	54.8884	0.2907	0.6859	0.1533	-0.1045	0.1223	0.5020	0.0039	0.1674	13.14	-0.02	0.02	7.65	0.05	73.71	14.94	0.10
935-01G	1.20	308.796	1.120	30.2732	0.2867	0.3647	0.1549	0.1044	0.1229	0.2713	0.0045	0.0923	7.25	0.03	0.04	7.52	0.09	73.78	14.69	0.18
935-01H	1.30	218.785	1.119	21.3320	0.2867	0.0511	0.1552	0.0014	0.1223	0.1917	0.0030	0.0651	5.11	0.00	0.05	7.57	0.12	73.84	14.78	0.24
935-01I	1.40	182.918	1.118	19.2456	0.2831	0.2473	0.1546	-0.1330	0.1219	0.1298	0.0035	0.0587	4.61	-0.06	0.06	7.48	0.14	78.78	14.61	0.26
935-01J	1.50	206.511	1.118	21.2149	0.2907	0.1260	0.1555	-0.1144	0.1219	0.1529	0.0029	0.0647	5.08	-0.05	0.05	7.58	0.12	77.88	14.80	0.24
935-01K	1.60	147.276	1.119	15.1330	0.2867	0.3211	0.1546	0.1265	0.1240	0.1024	0.0027	0.0461	3.62	0.08	0.07	7.71	0.17	79.28	15.06	0.34
935-01L	1.70	95.598	1.117	9.6699	0.2867	0.0941	0.1533	0.0800	0.1223	0.0722	0.0026	0.0295	2.32	0.07	0.11	7.66	0.27	77.48	14.95	0.52
935-01M	1.80	80.386	1.117	8.2910	0.2907	0.0964	0.1541	-0.0323	0.1223	0.0559	0.0026	0.0253	1.99	-0.04	0.13	7.68	0.32	79.21	14.99	0.61
935-01N	1.90	49.295	1.117	4.7594	0.2831	-0.0299	0.1538	-0.3136	0.1220	0.0383	0.0025	0.0145	1.14	-0.60	0.23	7.93	0.55	76.58	15.47	1.07
935-01O	2.00	54.211	1.117	6.1282	0.2811	-0.1713	0.1541	-0.0480	0.1210	0.0187	0.0024	0.0187	1.47	-0.07	0.18	7.93	0.42	89.64	15.47	0.82
935-01P	2.20	55.356	1.118	6.0897	0.2907	0.1770	0.1552	-0.0314	0.1240	0.0214	0.0025	0.0186	1.46	-0.05	0.18	8.04	0.44	88.47	15.69	0.86
935-01Q	2.40	70.621	1.117	9.1387	0.2868	0.2653	0.1539	0.2746	0.1230	0.0157	0.0024	0.0279	2.19	0.27	0.12	7.22	0.27	93.50	14.11	0.52
935-01R	2.60	30.366	1.116	3.9481	0.2831	0.0260	0.1536	-0.0096	0.1226	0.0038	0.0024	0.0120	0.95	-0.02	0.28	7.40	0.63	96.23	14.45	1.22
935-01S	2.80	10.451	1.117	1.2627	0.2832	0.1778	0.1552	-0.1076	0.1211	0.0009	0.0024	0.0039	0.30	-0.77	0.88	8.04	2.08	97.16	15.69	4.05
935-01T	3.00	5.756	1.116	0.6209	0.2780	0.0247	0.1531	0.1913	0.1237	0.0004	0.0024	0.0019	0.15	2.79	2.19	9.19	4.64	99.13	17.94	9.00
935-01U	4.00	43.946	1.115	5.2803	0.2828	-0.3493	0.1553	-0.1183	0.1223	0.0140	0.0024	0.0161	1.26	-0.20	0.21	7.52	0.47	90.38	14.68	0.92
M2, biotite^c; $J \pm 1\sigma = 0.001069 \pm 0.000002$; 9 m beneath the STD																				
952-01B	0.80	101.776	1.111	8.2870	0.2853	0.2962	0.1547	0.3559	0.1231	0.1318	0.0028	0.0253	6.91	0.37	0.13	7.54	0.31	61.46	14.70	0.60
952-01C	1.00	249.502	1.115	28.2200	0.2853	0.3470	0.1525	0.2578	0.1217	0.1157	0.0027	0.0861	23.53	0.08	0.04	7.62	0.09	86.19	14.84	0.18
952-01D	1.20	156.310	1.112	19.8956	0.2816	0.2718	0.1547	0.0162	0.1217	0.0254	0.0024	0.0607	16.59	0.01	0.05	7.47	0.13	95.15	14.56	0.24
952-01E	1.40	319.549	1.116	39.9163	0.2853	0.3560	0.1533	0.1820	0.1214	0.0519	0.0025	0.1217	33.29	0.04	0.03	7.61	0.06	95.17	14.84	0.12
952-01F	1.60	168.793	1.112	21.1467	0.2893	0.1414	0.1541	-0.2814	0.1211	0.0328	0.0025	0.0645	17.63	-0.11	0.05	7.51	0.12	94.14	14.63	0.23
952-01G	1.80	7.552	1.110	0.7744	0.2750	0.0077	0.1536	0.1590	0.1205	0.0032	0.0023	0.0024	0.65	1.76	1.47	8.57	3.49	87.90	16.69	6.76
952-01H	2.00	2.830	1.111	0.6881	0.2765	-0.0093	0.1528	0.0268	0.1231	-0.0009	0.0023	0.0021	0.57	0.33	1.54	4.53	2.63	110.09	8.83	5.13
952-01I	2.20	0.994	1.111	0.2769	0.2813	0.1538	0.1544	-0.0413	0.1211	-0.0020	0.0023	0.0008	0.23	-1.28	3.96	5.68	7.46	158.34	11.08	14.50
952-01J	2.40	2.013	1.110	0.7142	0.2780	-0.1233	0.1536	0.0065	0.1227	-0.0006	0.0023	0.0022	0.60	0.08	1.47	3.04	2.18	108.06	5.94	4.25
R05-06, amphibole^d; $J \pm 1\sigma = 0.001069 \pm 0.000002$; 24 m beneath the STD																				
951-01A	1.00	143.137	1.125	4.5910	0.2817	-0.0393	0.1566	0.6516	0.1241	0.1010	0.0027	0.0140	10.34	0.81	0.16	24.63	1.54	79.02	47.56	2.94
951-01B	1.50	391.222	1.132	19.9752	0.2880	0.5630	0.1581	35.1954	0.1234	0.2071	0.0039	0.0609	44.99	10.06	0.15	16.91	0.26	86.08	32.78	0.50
951-01C	1.90	291.858	1.126	15.2851	0.2879	0.4725	0.1563	27.8174	0.1259	0.1143	0.0036	0.0466	34.43	10.40	0.20	17.30	0.34	90.30	33.52	0.66
951-01D	2.30	54.445	1.126	4.5437	0.2843	0.0538	0.1546	5.6484	0.1237	0.0268	0.0025	0.0139	10.23	7.10	0.47	10.50	0.72	87.45	20.42	1.40
R05-09, biotite^e; $J \pm 1\sigma = 0.001069 \pm 0.000002$; 100 m beneath the STD																				
946-01B	0.65	27.333	1.109	1.9733	0.2848	0.3340	0.1544	-0.0129	0.1209	0.0679	0.0025	0.0060	0.71	-0.05	0.51	3.57	0.85	25.82	6.98	1.66
946-01C	0.80	191.136	1.113	14.6451	0.2888	0.0614	0.1538	0.0163	0.1222	0.3069	0.0033	0.0447	5.26	0.01	0.07	6.79	0.17	52.06	13.24	0.33
946-01D	0.90	296.860	1.113	32.9588	0.2848	0.3528	0.1538	0.0784	0.1205	0.1630	0.0029	0.1005	11.84	0.02	0.03	7.53	0.08	83.61	14.66	0.15
946-01E	1.00	256.999	1.114	31.5332	0.2848	0.3371	0.1541	0.1742	0.1229	0.0668	0.0026	0.0962	11.33	0.05	0.03	7.52	0.08	92.26	14.64	0.16
946-01F	1.10	225.541	1.113	27.2117	0.2848	0.1944	0.1550	-0.0145	0.1206	0.0606	0.0026	0.0830	9.78	0.00	0.04	7.62	0.09	91.97	14.84	0.18
946-01G	1.20	211.539	1.112	26.0454	0.2888	0.2821	0.1530	0.0764	0.1212	0.0570	0.0032	0.0794	9.36	0.02	0.04	7.47	0.10	91.96	14.54	0.19
946-01H	1.30	167.590	1.111	20.6662	0.2812	0.2823	0.1544	0.0687	0.1229	0.0479	0.0030	0.0630	7.42	0.03	0.05	7.41	0.12	91.47	14.45	0.24
946-01I	1.40	144.634	1.111	17.5961	0.2788	0.2693	0.1530	-0.0573	0.1206	0.0470	0.0030	0.0537	6.32	-0.03	0.06	7.42	0.14	90.29	14.45	0.28
946-01J	1.50	193.518	1.111	23.6787	0.2812	0.2396	0.1533	0.4477	0.1232	0.0483	0.0028	0.0722	8.51	0.16	0.04	7.57	0.11	92.61	14.74	0.21
946-01K	1.60	165.448	1.112	21.0078	0.2848	0.1008	0.1536	0.0764	0.1206	0.0337	0.0025	0.0641	7.55	0.03	0.05	7.39	0.12	93.92	14.40	0.23

Table 2. (continued)

Lab Run ID	CO ₂ Laser Power (W)	Measured Signals ($\times 10^{-15}$ A)					Derived Results													
		³⁹ Ar $\pm 1\sigma$	³⁸ Ar $\pm 1\sigma$	³⁷ Ar $\pm 1\sigma$	³⁶ Ar $\pm 1\sigma$	³⁹ Ar Mol ∞ 10 ⁻¹⁴ Total	Ca/K $\pm 1\sigma$	⁴⁰ Ar/ ³⁹ Ar $\pm 1\sigma$	% ⁴⁰ Ar*	Age (Ma) $\pm 1\sigma$										
946-01L	1.70	112.614	1.109	13.9363	0.2848	0.3585	0.1538	0.0584	0.1215	0.0216	0.0027	0.0425	5.01	0.04	0.07	7.62	0.18	94.31	14.84	0.36
946-01M	1.80	94.811	1.109	12.5346	0.2848	0.2280	0.1530	0.0852	0.1203	0.0119	0.0024	0.0382	4.50	0.06	0.08	7.28	0.20	96.29	14.18	0.38
946-01N	1.90	86.504	1.110	10.9670	0.2848	0.0463	0.1530	0.0783	0.1212	0.0134	0.0024	0.0334	3.94	0.06	0.09	7.52	0.23	95.39	14.65	0.44
946-01O	2.00	55.162	1.111	7.4104	0.2848	0.0265	0.1527	0.1598	0.1222	0.0075	0.0024	0.0226	2.66	0.18	0.14	7.15	0.33	96.05	13.93	0.63
946-01P	2.20	117.636	1.111	14.9867	0.2931	0.1566	0.1544	0.1059	0.1212	0.0170	0.0024	0.0457	5.38	0.06	0.07	7.51	0.17	95.70	14.63	0.33
946-01Q	2.40	13.403	1.108	1.2249	0.2778	-0.2701	0.1547	0.0872	0.1236	0.0035	0.0023	0.0037	0.44	0.60	0.86	10.10	2.53	92.29	19.64	4.89
R07-03, biotite^g; $J \pm 1\sigma = 0.001069 \pm 0.000002$; 104 m beneath the STD																				
948-01B	0.65	28.686	1.109	1.4691	0.2774	-0.3517	0.1545	0.0619	0.1203	0.0795	0.0026	0.0045	0.42	0.36	0.70	3.36	1.12	17.24	6.57	2.18
948-01C	0.80	252.166	1.112	14.7346	0.2850	0.5102	0.1539	0.6196	0.1213	0.5847	0.0042	0.0449	4.16	0.36	0.07	5.28	0.15	30.86	10.30	0.30
948-01D	0.90	197.005	1.114	17.0792	0.2850	0.2742	0.1545	0.3980	0.1216	0.2616	0.0031	0.0521	4.83	0.20	0.06	6.97	0.14	60.41	13.57	0.28
948-01E	1.00	228.939	1.112	23.0557	0.2814	0.2954	0.1540	0.3354	0.1213	0.1884	0.0031	0.0703	6.51	0.12	0.04	7.49	0.11	75.47	14.59	0.22
948-01F	1.10	231.632	1.112	25.7788	0.2814	0.5957	0.1551	0.4219	0.1210	0.1395	0.0037	0.0786	7.28	0.14	0.04	7.37	0.10	82.08	14.36	0.20
948-01G	1.20	457.937	1.118	48.3847	0.2890	0.5844	0.1548	0.5110	0.1226	0.3239	0.0048	0.1475	13.67	0.09	0.02	7.47	0.06	78.91	14.54	0.11
948-01H	1.30	227.995	1.113	24.8882	0.2851	0.3692	0.1534	0.2845	0.1226	0.1492	0.0038	0.0759	7.03	0.10	0.04	7.37	0.11	80.51	14.36	0.21
948-01I	1.40	376.820	1.116	40.3079	0.2890	0.4499	0.1546	0.2351	0.1213	0.2518	0.0030	0.1229	11.39	0.05	0.03	7.48	0.06	80.07	14.58	0.12
948-01J	1.50	286.787	1.116	32.0949	0.2851	0.3908	0.1555	0.3517	0.1213	0.1585	0.0028	0.0979	9.07	0.09	0.03	7.46	0.08	83.53	14.54	0.15
948-01K	1.60	195.977	1.111	22.7166	0.2851	0.3550	0.1534	0.1328	0.1204	0.0962	0.0027	0.0693	6.42	0.05	0.04	7.36	0.11	85.37	14.34	0.21
948-01L	1.70	141.599	1.113	16.3068	0.2933	-0.1389	0.1555	0.2648	0.1213	0.0690	0.0026	0.0497	4.61	0.14	0.06	7.42	0.16	85.49	14.46	0.30
948-01M	1.80	165.078	1.110	19.1820	0.2851	-0.1910	0.1531	-0.0213	0.1213	0.0654	0.0026	0.0585	5.42	-0.01	0.05	7.58	0.13	88.16	14.77	0.26
948-01N	1.90	142.780	1.111	17.0550	0.2851	0.3963	0.1540	0.2820	0.1223	0.0531	0.0025	0.0520	4.82	0.14	0.06	7.44	0.15	88.96	14.50	0.29
948-01O	2.00	104.356	1.112	12.4683	0.2851	0.1805	0.1543	0.0281	0.1213	0.0378	0.0025	0.0380	3.52	0.02	0.08	7.46	0.20	89.18	14.54	0.39
948-01P	2.20	222.262	1.113	26.4385	0.2851	0.1743	0.1543	0.6911	0.1230	0.0716	0.0027	0.0806	7.47	0.22	0.04	7.60	0.10	90.48	14.81	0.19
948-01Q	2.40	74.152	1.112	8.3206	0.2851	0.1817	0.1534	0.0407	0.1210	0.0152	0.0024	0.0254	2.35	0.04	0.12	8.36	0.33	93.88	16.28	0.63
948-01R	2.60	22.795	1.112	2.2625	0.2891	-0.0640	0.1546	-0.1507	0.1216	0.0024	0.0023	0.0069	0.64	-0.56	0.46	9.73	1.37	96.66	18.94	2.66
948-01S	2.80	10.065	1.110	1.3893	0.2851	0.1083	0.1537	0.1644	0.1213	-0.0001	0.0023	0.0042	0.39	1.00	0.77	7.31	1.77	100.86	14.23	3.44
R07-05, biotite^g; $J \pm 1\sigma = 0.001069 \pm 0.000002$; 109 m beneath the STD																				
947-01B	0.65	14.542	1.108	0.5020	0.2740	-0.1474	0.1545	-0.3011	0.1229	0.0412	0.0025	0.0015	0.18	-5.03	3.43	4.25	3.51	14.69	8.29	6.84
947-01C	0.80	129.314	1.110	6.6403	0.2849	0.3183	0.1530	0.2453	0.1222	0.2944	0.0035	0.0202	2.32	0.31	0.16	6.25	0.35	32.10	12.18	0.69
947-01D	0.90	158.294	1.110	13.4208	0.2889	0.3419	0.1528	0.1012	0.1206	0.1890	0.0030	0.0409	4.69	0.06	0.08	7.59	0.19	64.38	14.79	0.38
947-01E	1.00	161.086	1.111	16.8523	0.2889	-0.1293	0.1539	-0.1279	0.1226	0.1141	0.0028	0.0514	5.89	-0.06	0.06	7.53	0.15	78.81	14.67	0.30
947-01F	1.10	172.409	1.110	19.2021	0.2813	0.1202	0.1536	0.2815	0.1209	0.0812	0.0026	0.0586	6.71	0.12	0.05	7.72	0.17	85.99	15.03	0.36
947-01G	1.20	141.176	1.110	15.6016	0.2849	0.1537	0.1531	0.1564	0.1219	0.0594	0.0025	0.0476	5.45	0.08	0.07	7.91	0.17	87.48	15.41	0.33
947-01H	1.30	191.154	1.110	21.0449	0.2849	0.4884	0.1545	0.2579	0.1222	0.0904	0.0026	0.0642	7.36	0.10	0.05	7.80	0.12	85.93	15.20	0.24
947-01I	1.40	181.899	1.113	20.0823	0.2849	0.2361	0.1539	-0.0134	0.1226	0.0791	0.0027	0.0612	7.02	-0.01	0.05	7.88	0.13	87.01	15.34	0.25
947-01J	1.50	184.439	1.111	19.6971	0.2773	0.0973	0.1548	-0.0004	0.1226	0.0986	0.0027	0.0601	6.88	0.00	0.05	7.86	0.13	84.04	15.32	0.25
947-01K	1.60	191.343	1.111	20.8901	0.2850	0.2836	0.1551	0.1859	0.1206	0.0901	0.0027	0.0637	7.30	0.07	0.05	7.87	0.13	85.97	15.33	0.24
947-01L	1.70	197.515	1.111	21.8926	0.2850	0.2563	0.1531	0.2014	0.1216	0.0906	0.0027	0.0668	7.65	0.08	0.05	7.78	0.12	86.33	15.16	0.23
947-01M	1.80	247.923	1.113	28.6075	0.2850	0.3165	0.1545	-0.0628	0.1229	0.0819	0.0027	0.0682	10.00	-0.02	0.04	7.81	0.09	90.13	15.21	0.18
947-01N	1.90	177.682	1.111	20.9499	0.2810	0.3364	0.1539	0.1073	0.1209	0.0475	0.0026	0.0639	7.32	0.04	0.05	7.80	0.12	92.03	15.20	0.24
947-01O	2.00	110.589	1.109	12.8721	0.2850	0.4552	0.1539	0.1514	0.1226	0.0243	0.0024	0.0393	4.50	0.10	0.08	8.03	0.21	93.48	15.64	0.40
947-01P	2.20	261.399	1.112	31.3298	0.2850	0.3253	0.1542	-0.0524	0.1219	0.0461	0.0026	0.0955	10.95	-0.01	0.03	7.90	0.08	94.73	15.39	0.16
947-01Q	2.40	140.706	1.111	16.5043	0.2850	0.0817	0.1539	0.0643	0.1226	0.0222	0.0024	0.0503	5.77	0.03	0.06	8.12	0.16	95.30	15.82	0.31
R07-07, biotite^h; $J \pm 1\sigma = 0.001069 \pm 0.000002$; 134 m beneath the STD																				
945-01F	1.10	375.212	1.115	47.2029	0.2847	0.7115	0.1550	0.0075	0.1218	0.0550	0.0026	0.1439	15.01	0.00	0.02	7.60	0.05	95.62	14.80	0.10
945-01G	1.20	95.965	1.109	12.3123	0.2929	0.3588	0.1544	-0.2128	0.1215	0.0149	0.0024	0.0375	3.92	-0.14	0.08	7.42	0.21	95.30	14.46	0.40

Table 2. (continued)

Lab Run ID	CO ₂ Laser Power (W)	Measured Signals ($\times 10^{-15}$ A)					Derived Results													
		⁴⁰ Ar $\pm 1\sigma$	³⁹ Ar $\pm 1\sigma$	³⁸ Ar $\pm 1\sigma$	³⁷ Ar $\pm 1\sigma$	³⁶ Ar $\pm 1\sigma$	³⁹ Ar Mol $_{10-14}^{\infty}$	³⁹ Ar % of Total	Ca/K $\pm 1\sigma$	⁴⁰ Ar/ ³⁹ Ar $\pm 1\sigma$	% ⁴⁰ Ar *	Age (Ma) $\pm 1\sigma$								
945-01H	1.30	134.194	1.109	16.6190	0.2810	0.0355	0.1529	-0.2611	0.1218	0.0216	0.0024	0.0507	5.29	-0.13	0.06	7.68	0.15	95.13	14.96	0.30
945-01I	1.40	221.361	1.111	27.9049	0.2847	0.4545	0.1535	0.0937	0.1225	0.0419	0.0025	0.0851	8.88	0.04	0.04	7.48	0.09	94.37	14.58	0.18
945-01J	1.50	206.141	1.111	26.3820	0.2847	0.4818	0.1529	0.1776	0.1221	0.0322	0.0024	0.0804	8.39	0.06	0.04	7.45	0.09	95.36	14.51	0.18
945-01K	1.60	255.326	1.111	31.9465	0.2847	0.6899	0.1529	-0.0965	0.1211	0.0442	0.0025	0.0974	10.16	-0.03	0.03	7.57	0.08	94.82	14.76	0.15
945-01L	1.70	179.284	1.109	23.2081	0.2787	0.3423	0.1527	-0.0131	0.1218	0.0205	0.0024	0.0708	7.38	0.00	0.04	7.46	0.11	96.59	14.53	0.21
945-01M	1.80	232.662	1.111	29.8315	0.2847	0.2667	0.1553	0.0765	0.1232	0.0209	0.0024	0.0910	9.49	0.02	0.03	7.59	0.08	97.33	14.78	0.16
945-01N	1.90	169.194	1.110	21.7592	0.2804	0.2469	0.1573	-0.0847	0.1199	0.0121	0.0024	0.0664	6.92	-0.03	0.05	7.60	0.12	97.85	14.82	0.22
945-01O	2.00	85.948	1.110	10.8991	0.2847	0.1702	0.1563	0.0559	0.1221	0.0043	0.0023	0.0332	3.47	0.04	0.09	7.76	0.24	98.51	15.13	0.46
945-01P	2.20	157.631	1.111	20.5378	0.2848	0.4663	0.1553	-0.0320	0.1236	0.0072	0.0024	0.0626	6.53	-0.01	0.05	7.57	0.12	98.63	14.74	0.24
945-01Q	2.40	146.073	1.109	19.0870	0.2811	0.4318	0.1550	0.0051	0.1215	0.0071	0.0024	0.0582	6.07	0.00	0.05	7.54	0.13	98.55	14.69	0.25
945-01R	2.60	89.759	1.109	11.6692	0.2848	0.1758	0.1538	0.0017	0.1218	0.0024	0.0023	0.0356	3.71	0.00	0.09	7.63	0.22	99.20	14.86	0.42
945-01S	2.79	69.246	1.109	9.4687	0.2930	0.0221	0.1541	-0.2497	0.1212	0.0029	0.0024	0.0289	3.01	-0.22	0.11	7.21	0.26	98.64	14.05	0.51
945-01T	1.77	34.236	1.108	4.0821	0.2797	0.1694	0.1544	0.1620	0.1215	0.0023	0.0024	0.0124	1.30	0.33	0.25	8.23	0.65	98.12	16.02	1.26
945-01U	4.00	12.227	1.109	1.4900	0.2811	-0.1230	0.1535	0.0665	0.1225	-0.0009	0.0023	0.0045	0.47	0.37	0.69	8.40	1.81	102.40	16.36	3.52

R07-08, biotite; $J \pm 1\sigma = 0.001069 \pm 0.000002$; 156 m beneath the STD

949-01B	0.65	5.944	1.110	0.5197	0.2805	0.0222	0.1540	0.3006	0.1223	0.0125	0.0024	0.0016	0.22	4.92	3.32	4.45	3.49	38.84	8.68	6.80
949-01C	0.80	113.154	1.111	8.6660	0.2852	0.2508	0.1535	0.1010	0.1204	0.1510	0.0028	0.0264	3.71	0.10	0.12	7.86	0.30	60.20	15.30	0.59
949-01D	0.90	304.614	1.117	32.0136	0.2891	0.7448	0.1537	-0.2385	0.1210	0.1783	0.0030	0.0976	13.71	-0.06	0.03	7.85	0.08	82.50	15.28	0.16
949-01E	1.00	206.981	1.113	24.1325	0.2852	0.2193	0.1552	0.0673	0.1213	0.0559	0.0026	0.0736	10.34	0.02	0.04	7.88	0.11	91.95	15.35	0.21
949-01F	1.10	188.744	1.112	23.2776	0.2815	0.4790	0.1537	0.0575	0.1223	0.0308	0.0024	0.0710	9.97	0.02	0.04	7.71	0.11	95.14	15.02	0.21
949-01G	1.20	134.593	1.112	16.4312	0.2852	0.1092	0.1532	-0.0507	0.1213	0.0196	0.0024	0.0501	7.04	-0.03	0.06	7.83	0.16	95.65	15.25	0.31
949-01H	1.30	135.343	1.112	16.4114	0.2852	0.3523	0.1540	0.0839	0.1217	0.0226	0.0027	0.0500	7.03	0.04	0.06	7.83	0.16	95.04	15.26	0.31
949-01I	1.40	105.586	1.111	13.1668	0.2852	-0.2529	0.1538	-0.2127	0.1227	0.0183	0.0026	0.0402	5.64	-0.14	0.08	7.59	0.19	94.75	14.79	0.38
949-01J	1.50	162.658	1.111	19.8261	0.2852	0.1074	0.1555	0.4318	0.1207	0.0278	0.0025	0.0605	8.49	0.19	0.05	7.79	0.13	94.98	15.17	0.25
949-01K	1.60	128.418	1.111	15.8910	0.2852	-0.0094	0.1552	0.2093	0.1213	0.0217	0.0024	0.0485	6.81	0.11	0.07	7.67	0.16	95.00	14.95	0.31
949-01L	1.70	149.324	1.110	18.3680	0.2779	0.1661	0.1543	0.0048	0.1213	0.0254	0.0024	0.0560	7.87	0.00	0.06	7.71	0.14	94.91	15.02	0.27
949-01M	1.80	138.842	1.112	16.7346	0.2852	0.1345	0.1538	-0.1043	0.1223	0.0251	0.0028	0.0510	7.17	-0.05	0.06	7.84	0.16	94.58	15.28	0.31
949-01N	1.90	106.754	1.112	13.3420	0.2934	-0.0080	0.1541	0.2691	0.1217	0.0148	0.0024	0.0407	5.72	0.17	0.08	7.67	0.20	95.92	14.94	0.38
949-01O	2.00	116.410	1.111	14.6405	0.2892	0.4589	0.1532	0.0714	0.1220	0.0131	0.0024	0.0446	6.27	0.04	0.07	7.68	0.18	96.67	14.97	0.34

^aAll data corrected for blanks, radioactive decay, nucleogenic interferences, mass discrimination, and detector intercalibration. Ages calculated with decay constants in Min et al. [2000], atmospheric ⁴⁰Ar/³⁶Ar = 298.56 ± 0.31 [Lee et al., 2006], and age of 28.201 ± 0.046 for Fish Canyon sanidine [Kuiper et al., 2008]. Argon isotope data for all samples acquired by simultaneous collection of all masses on Faraday collectors (40–37) and ion counter (36) with a Thermo Scientific ARGUSVI mass spectrometer. Errors on ⁴⁰Ar/³⁹Ar plateau and integrated ages are 2 σ .

- ^bPlateau age = 14.89 ± 0.07 Ma, steps 0.8–4.0 W, 100% of ³⁹Ar, MSWD = 0.4, and integrated age = 14.89 ± 0.07 Ma.
- ^cPlateau age = 14.77 ± 0.17 Ma, steps 0.8–2.2 W, 99.4% of ³⁹Ar, MSWD = 0.4, and integrated age = 14.77 ± 0.17 Ma.
- ^dPlateau age = 33.0 ± 0.8 Ma, steps 1–1.9 W, 79.4% of ³⁹Ar, MSWD = 0.8, and integrated age = 32 ± 4 Ma.
- ^ePlateau age = 14.61 ± 0.13 Ma, steps 0.9–2.4 W, 94% of ³⁹Ar, MSWD = 0.6, and integrated age = 14.6 ± 0.2 Ma.
- ^fPlateau age = 14.54 ± 0.11 Ma, steps 1.0–2.2 W, 87.2% of ³⁹Ar, MSWD = 0.5, and integrated age = 14.4 ± 0.4 Ma.
- ^gPlateau age = 15.25 ± 0.13 Ma, steps 0.9–2.4 W, 97.5% of ³⁹Ar, MSWD = 0.9, and integrated age = 15.23 ± 0.19 Ma.
- ^hPlateau age = 14.72 ± 0.11 Ma, steps 1.1–4.0 W, 100% of ³⁹Ar, MSWD = 0.6, and integrated age = 14.72 ± 0.11 Ma.
- ⁱPlateau age = 15.16 ± 0.15 Ma, steps 0.6–2.0 W, 100% of ³⁹Ar, MSWD = 0.4, and integrated age = 15.16 ± 0.15 Ma.

increase progressively toward metamorphic values ($\delta D_{\text{biotite}} > -100\text{‰}$) toward the base of the exposed footwall section. This trend is consistent with low δD values acquisition by isotopic exchange between minerals and meteoric fluids during activity of the detachment system, including mylonitic deformation and recrystallization in the immediate footwall of the detachment, although postdeformation hydrogen isotope exchange cannot be totally ruled out.

- $^{40}\text{Ar}/^{39}\text{Ar}$ geochronology yields middle Miocene plateau ages over the same ~ 200 m of structural section. We interpret these ages to represent cooling ages from which, together with published U-Pb data [Hodges *et al.*, 1998; Murphy and Harrison, 1999; Searle *et al.*, 2003; Cottle *et al.*, 2015], we can estimate a minimum duration of deformation-controlled hydrogen isotope exchange between meteoric fluids and (re)-crystallized syntectonic silicate minerals of less than 2 Myr (~ 16.7 – 14.9 Ma).

Although a number of geodynamic models have been proposed to explain the exhumation of lower to middle crustal rocks in association with normal-sense motion on the STD, none of these models have highlighted the potential importance of fluids, as recorded by stable isotopes from shear zones, during extensional tectonics/normal faulting in the Tethyan sedimentary rocks that form the hanging wall to the STD. We propose that the influx of meteoric water into the STD system was facilitated by brittle faulting and extension of these upper crustal hanging wall rocks.

6.1. Interpretation of δD Values

Low δD values of biotite, muscovite, chlorite, and hornblende grains ($\delta D_{\text{silicate}} < -126\text{‰}$) from schist, calc-silicate, and leucogranite characterize the STD footwall at distances of 9–35 m and 97–109 m beneath the detachment (Figure 3 and Table 1). Such negative δD values suggest the presence of low- δD meteoric water associated with the growth of these synkinematic hydrous minerals during high-temperature penetrative deformation in the STD footwall (see below). In addition, as highlighted by $\delta D_{\text{biotite}}$ values that range from -126‰ to -182‰ , these minerals interacted to various degrees with meteoric fluids that were most likely sourced at high elevation [e.g., Taylor, 1990]. In contrast, leucogranite samples collected from the top 9 m of STD footwall, as well as at 40–41 m beneath the detachment, contain muscovite grains that have higher δD values ranging from -80 to -100‰ and from -77 to -98‰ , respectively. Similarly, biotite grains in leucogranites collected at 40–41 m have higher δD values (-129‰) than those usually observed in the surrounding metasedimentary rocks, reflecting only moderate interaction with surface-derived fluids (Figure 3 and Table 1). Below the 109 m depth interval, schist, gneiss, and calc-silicate samples that form the base of the section provide high $\delta D_{\text{biotite}}$ values ranging from -85 to -97‰ (Figure 3 and Table 1) that indicate a signature again dominated by metamorphic fluids.

The δD data suggest that during development of the observed deformation microstructures, the footwall rocks interacted with surface-derived fluids down to present-day depths of 109 m beneath the STD. We view the variations in δD values within the structural section as reflecting the result of time-integrated hydrogen isotope exchange between water and rock controlled by the depth to which meteoric fluids were able to penetrate beneath the detachment, which was itself probably modulated by the contrast in permeability of the different rock types (principally metasedimentary rocks versus leucogranites).

Using a deformation and isotopic exchange temperature of $\sim 580 \pm 50^\circ\text{C}$ inferred from the opening angles of quartz *c* axis fabric girdles from the mylonitic footwall leucogranites [Law *et al.*, 2011], combined with the calibration for hydrogen isotope exchange between biotite and water [Suzuoki and Epstein, 1976], biotite grains from leucogranites within the top ~ 100 m of STD footwall yield δD_{water} values as low as $-150 \pm 5/-4\text{‰}$ (Figure 3 and Table 1). Similarly, hornblende separates from calc-silicates give low δD_{water} values of $-155 \pm 5\text{‰}$ using a deformation temperature of $\sim 540 \pm 50^\circ\text{C}$ [Law *et al.*, 2011] and the Suzuoki and Epstein [1976] calibration for hydrogen isotope hornblende-water fractionation. Biotite grains from schist and calc-silicate samples provide very consistent results with δD_{water} values as low as -141‰ (Figure 3 and Table 1). In contrast, δD_{water} values calculated for muscovite are typically less negative ranging from $-65 \pm 4\text{‰}$ to $-118 \pm 4\text{‰}$ using the same deformation temperatures determined by Law *et al.* [2011] for mylonitic leucogranite from the Northern Transect (Figure 3 and Table 1) and the muscovite-water-hydrogen isotope exchange equations of Suzuoki and Epstein [1976].

The δD values of muscovite vary with grain size (Figure 3). This is also reflected in the δD_{water} values calculated for samples R-05-04 and R-03-24 for which the largest grain size ($f > 500 \mu\text{m}$) yields δD_{water} values 14 and

20‰ higher, respectively, when compared to the smallest fraction ($250 < f < 500 \mu\text{m}$) (Table 1). The larger muscovite grains, characterized by lenticular mica fish or fish with small aspect ratios (Figure 2a), may be older grains from the protolith that did not (completely) recrystallize in the presence of meteoric fluids in the STD footwall during high-temperature shearing. In contrast, smaller grains that formed by solution-precipitation in strain shadows of porphyroclasts (Figure 2b) and/or crystallized parallel to foliation or shear bands equilibrated with surface-derived fluids during deformation. However, this grain size dependence is not observed for biotite (see sample R-07-03 or R-07-05, Table 1). This difference for muscovite grains could be related to texture, composition, and permeability of the rock; leucogranite samples display, on average, higher δD_{water} values than those calculated for biotite-schist and calc-silicate samples and/or a different hydrogen isotope exchange mechanism in biotite and muscovite. One alternative interpretation is that the syntectonic 17–16 Ma leucogranites [Hodges *et al.*, 1998; Murphy and Harrison, 1999; Searle *et al.*, 2003] were susceptible to deformation-induced recrystallization and therefore fluid-rock exchange, for only a relatively short time compared to the metasedimentary host rocks.

6.2. Timing of Fluid Flow and Deformation

We have established $^{40}\text{Ar}/^{39}\text{Ar}$ ages for multigrain biotite separates showing low δD values ($-163\text{‰} \leq \delta D_{\text{biotite}} \leq -135\text{‰}$) from the top 9–109 m of the STD footwall. All of these separates display constant $^{40}\text{Ar}/^{39}\text{Ar}$ ages of ~ 15 Ma from the top to the bottom of the section. The $^{40}\text{Ar}/^{39}\text{Ar}$ thermochronology conducted on biotite separates that were collected toward the base of the section, where interaction with surface-derived fluids was minimal ($\delta D_{\text{biotite}} \sim -85\text{‰}$), yield similar ~ 15 Ma ages. Schultz *et al.* [2017] have reported similar $^{40}\text{Ar}/^{39}\text{Ar}$ cooling ages (15.4–14.4 Ma) for white mica grains in samples of leucogranite collected from the footwall of the STD in the Rongbuk Valley in outcrops located ~ 7 –20 km to the south of our Northern Transect. Additionally, Carrapa *et al.* [2016, Table DR.4] also report similar $^{40}\text{Ar}/^{39}\text{Ar}$ ages for white mica grains (~ 16.5 –14.9 Ma) in river sands from the Rongbuk Valley that have presumably been eroded from these footwall rocks.

In biotite-schist sample M2 (9 m beneath the detachment), very similar $^{40}\text{Ar}/^{39}\text{Ar}$ ages were obtained on biotite (14.77 ± 0.17 Ma) and muscovite (14.89 ± 0.07 Ma) grains from a foliation-parallel syntectonic muscovite-bearing pegmatite vein. This similarity in biotite and muscovite $^{40}\text{Ar}/^{39}\text{Ar}$ ages suggests that the pegmatite underwent rapid cooling, considering estimated closure temperatures of $335 \pm 50^\circ\text{C}$ for biotite [Harrison *et al.*, 1985] and $\geq 400 \pm 50^\circ\text{C}$ for muscovite [Hames and Bowring, 1994; Harrison *et al.*, 2009]. However, while biotite and muscovite yield similar ages at ~ 15 Ma, they have different δD values ($\delta D_{\text{biotite}} = -156\text{‰}$ and $\delta D_{\text{muscovite}} = -100\text{‰}$). The biotite undoubtedly recrystallized in the presence of meteoric water ($\delta D_{\text{water}} = -124 \pm 4\text{‰}$), while the muscovite ($\delta D_{\text{water}} = -89 \pm 4\text{‰}$) displays either only moderate exchange with meteoric fluids or interaction with fluids that had a mixed meteoric-magmatic source. Considering that, for the same temperature, biotite and muscovite show a $\sim 20\text{‰}$ difference in hydrogen isotope fractionation (lower for biotite) and that the STD footwall at this structural distance beneath the detachment (9 m) was infiltrated by meteoric fluids, we would have expected $\delta D_{\text{muscovite}}$ values as low as -136‰ . Instead, we obtained a $\delta D_{\text{muscovite}}$ value $\sim 36\text{‰}$ higher ($\delta D_{\text{muscovite}} = -100\text{‰}$). We note that both biotite and muscovite from sample M2 have appropriate water concentrations ($\text{H}_2\text{O}_{\text{wt}}\% = 4.14$ (Bt), $\text{H}_2\text{O}_{\text{wt}}\% = 4.26$ (Ms)) for their mineral chemistries (see Text 1 of supporting information for explanation of calculations; Gong *et al.* [2007]). Differences in δD values and similarities in $^{40}\text{Ar}/^{39}\text{Ar}$ ages highlight a lack of correlation between hydrogen and ^{40}Ar isotope exchange.

Two lines of evidence indicate that hydrogen isotope exchange between biotite grains and meteoric fluids occurred during grain-scale deformation. (1) Elongate lenticular biotite fish [Ten Grotenhuis *et al.*, 2003] indicate a top-to-north sense of shear (Figure 2e). Formation of mica fish involves recrystallization by solution-precipitation where mica dissolution and element transport via a fluid phase enable new biotite growth [e.g., Dunlap, 1992; Mulch *et al.*, 2005; Gébelin *et al.*, 2011]. (2) Biotite fish record low $\delta D_{\text{biotite}}$ values within the top 109 m of the STD footwall, requiring exchange with low- δD meteoric water during mylonitization. Similarly, muscovite grains display recrystallized tails with a top-north sense of shear that are, however, not necessarily associated with low $\delta D_{\text{muscovite}}$ values.

As also suggested by previous studies in the Everest area [e.g., Streule *et al.*, 2012], we interpret our $^{40}\text{Ar}/^{39}\text{Ar}$ ages obtained on biotite and muscovite grains in terms of cooling through the appropriate closure

temperatures at ~15 Ma, with isotopic exchange between hydrous minerals and meteoric fluids occurring shortly before that time. The syntectonic intrusive pegmatite vein (sample M2) represents an excellent marker of incremental deformation and provides key information on the timing and duration of isotopic exchange. Published U-Pb data indicate that leucogranite intrusion and penetrative shearing was active along the Rongbuk segment of the STD at ~16.7 Ma [Hodges *et al.*, 1998; Murphy and Harrison, 1999; Searle *et al.*, 2003; Cottle *et al.*, 2015] and that movement had ceased prior to 15.6 Ma [Cottle *et al.*, 2015]. In addition, despite a ~70°C difference in nominal closure temperature (see below), biotite and muscovite grains yield similar ages, suggesting that rapid cooling ensued at ~15 Ma. Following high-temperature syntectonic foliation-parallel emplacement of pegmatite (temperature above the closure temperature of the $^{40}\text{Ar}/^{39}\text{Ar}$ system in biotite and muscovite), we propose that at ~15 Ma both sheared leucogranites and metasedimentary rocks cooled rapidly through the closure temperature of argon in muscovite ($\geq 400 \pm 50^\circ\text{C}$; Hames and Bowring [1994] and Harrison *et al.* [2009]) and biotite ($335 \pm 50^\circ\text{C}$; Harrison *et al.* [1985]). In contrast to biotite grains from the host metasedimentary rocks that likely exchanged with surface-derived fluids before pegmatite intrusion, we suggest that muscovite grains in the pegmatite with a $^{40}\text{Ar}/^{39}\text{Ar}$ age of 14.89 ± 0.07 Ma (sample M2) and $\delta\text{D}_{\text{muscovite}}$ of -100‰ interacted with surface-derived fluids for only a short time period. As a consequence, based on our $^{40}\text{Ar}/^{39}\text{Ar}$ data and U-Pb data acquired previously on leucogranites from Rongbuk [Hodges *et al.*, 1998; Murphy and Harrison, 1999; Searle *et al.*, 2003; Cottle *et al.*, 2015], we suggest that hydrogen isotopic exchange between meteoric fluids and minerals occurred (1) prior to 15 Ma and yet (2) after intrusion of the earliest leucogranites in the Rongbuk STD footwall at ~16.7 Ma. One or two million years (between 16.7 and 14.9 Ma) would, therefore, represent the minimum duration of hydrogen isotopic exchange. However, this does not preclude the possibility that fluid infiltration and detachment activity may have occurred before ~16.7 Ma but rather that the δD values we measure in the leucogranites/pegmatites were likely acquired during this time interval.

In contrast to biotite and muscovite, hornblende from a calc-silicate layer at 24 m beneath the detachment (sample R-05-06) provides an older $^{40}\text{Ar}/^{39}\text{Ar}$ plateau age of 33.0 ± 0.8 Ma. The hornblende in this sample displays a low δD value of -183‰ . Hornblende occurs as elongate grains with recrystallization tails oriented parallel to the foliation (Figure 2c), a textural relation also displayed by biotite fish with a low δD value (-174‰) in the same sample, suggesting that both minerals exchanged with deuterium-depleted meteoric fluids during deformation.

In contrast to biotite, the hornblende grains that show a complex ^{39}Ar release spectrum could be related to partial resetting during deformation and infiltration of meteoric fluids and in that case would suggest that the deformation temperature that affected the calc-silicate layer ($\sim 545 \pm 50^\circ\text{C}$ estimated from quartz *c* axis fabric opening angles; Law *et al.* [2011], their samples R-03-15, 16, 18, and 19 from the Northern Transect) was slightly below the argon closure temperature of hornblende ($\sim 530 \pm 40^\circ\text{C}$; Harrison [1981]). This age spectrum could also reflect chemical zonation of hornblende and/or the presence of exsolution features [e.g., Harrison and Fitz Gerald, 1986].

6.3. Tectonic Implications

Hydrogen isotope ratios of silicate minerals that formed in the STD footwall in the Mount Everest region indicate that meteoric water penetrated down to the ductile crust at least between 16.7 and 14.9 Ma during high-temperature deformation. The presence of low- δD meteoric water in the STD footwall raises the question of how these fluids penetrated the crust down to the ductile segment of the STD during the middle Miocene. We propose that the presence of these fluids in the STD footwall is consistent with a model involving synconvergent stretching/extension of the upper crust, high (paleo-) geothermal gradient, and high topography.

If stretching/extension did occur in the Tethyan Himalayan sequence during top-to-the-north normal-sense motion on the underlying STD, the activation of normal faults and the prevalence of open vertical fractures would likely have enhanced porosity and permeability, creating conduits for fluid flow from the Earth's surface down to the detachment system. In general, downward penetration of meteoric fluids is limited when the upper crust is in compression [Nesbitt and Muehlenbachs, 1995; Pollyea *et al.*, 2015] but is enhanced during regional extension [Person *et al.*, 2007]. Additional heat input coeval with exhumation of the STD footwall would favor buoyancy-driven, convective fluid flow and hence transport of meteoric water to significant depths. Finally, high surface topography creates the necessary hydraulic head, especially in regions of high relief, for surface-derived fluids to penetrate to deep levels of the continental crust. In the Himalaya, the

combination of open fractures, high thermal gradient, and topography/hydraulic head would have generated the necessary sustained fluid flow over the timescale of motion on the STD to promote (deep) circulation of meteoric fluids.

It seems likely that these three conditions for promoting extension-related fluid flow in the upper crust (syn-convergent stretching/extension of the upper crust, high (paleo-) geothermal gradient, and high topography) were met in the Himalaya during the middle Miocene. High heat flow would have been provided by crustal thickening, partial melting, and intrusion of leucogranites in the STD footwall [Hodges *et al.*, 1998; Murphy and Harrison, 1999], and a topographic high characterized the Mount Everest region [Gébelin *et al.*, 2013] and southern Tibet [Spicer *et al.*, 2003; Ding *et al.*, 2017] at that time. Of critical importance, this model for flow of meteoric water through the Tethyan sedimentary rocks down to the STD also requires the presence of normal faults in the Tethyan hanging wall rocks that sole down on to the STD and were demonstrably active at the same time (~15 Ma) as normal-sense shearing on the STD. At least within the Everest area, the transport direction indicated by mineral stretching lineations and quartz *c* axis fabrics for normal-sense motion on the STD is ~030° (i.e., N30°E, Carosi *et al.* [1998] and Law *et al.* [2011]), and presumably the suggested hanging wall normal faults would strike at a high angle to this transport direction [e.g., Wernicke and Burchfiel, 1982]. At least one high-angle normal fault striking 120° has been mapped displacing lithologic units within the Tethyan rocks lying above the STD to the south of the Northern Transect (Figures 1c and 1d; Chi-Hsiang and Shih-Tseng [1978]). Several other similarly oriented normal faults were mapped cutting Tethyan sedimentary rocks and in ~E-W trending valleys to the north of the Northern Transect (Figure 1b).

Burchfiel *et al.* [1992] in their seminal reconnaissance study of the STD exposed in the central eastern Himalaya and adjacent Tibetan Plateau mapped a number of normal faults within the Tethyan rocks striking at a high angle to the STD transport direction (Figure 1b). In some cases these faults were interpreted as cross-cutting and down-dropping local strands of the STD to the north (e.g., Rongbuk Valley), while in other cases the normal faults soled into the underlying STD [see Burchfiel *et al.*, 1992, Figure 25]. They were unsure if “these faults are part of separate detachment systems or whether they form hanging wall splays that merge at depth into the South Tibetan detachment system” [see Burchfiel *et al.*, 1992, p. 37].

It should also be kept in mind that if there were normal faults acting as conduits for meteoric water penetrating down to the STD mylonitic footwall rocks that were deforming at ~500–600°C and are now exposed in the Rongbuk Valley, these would not have been the faults in the unmetamorphosed Tethyan sedimentary rocks that now overlie exposures of the footwall at Rongbuk (Figures 1c and 1d). Such faults would be located farther to the north, with the distance depending on factors such as the dip and amount of slip on the STD. Geologic mapping indicates an absolute minimum normal-sense displacement of ~35 km on the STD in the Everest region [see Burchfiel *et al.*, 1992, p. 20]. Searle *et al.* [2002, 2003] calculated a total slip of ~100–200 km (depending on assumed regional dip of the detachment) on the STD in the Everest region based on barometry of metamorphic mineral assemblages in HCC rocks in the footwall to the STD. Subsequently, Law *et al.* [2011] estimated normal-sense slip values of between 25 and 170 km using particle path models based on the apparent telescoping of synkinematic isotherms associated with plastic deformation of HCC footwall rocks exposed in the Rongbuk Valley. Law *et al.* [2011] noted that their slip estimates largely refer to the portion of motion on the STD accommodated by high-temperature ductile deformation, whereas the higher values estimated by Searle *et al.* [2002, 2003] are for total offset and include both ductile and brittle deformation. If these estimates are valid, then clearly the normal faults originally feeding meteoric waters down to the plastically deforming footwall rocks now exposed at Rongbuk would have been located far to the north of the Rongbuk Valley.

Several models involving different crustal and mantle processes have been proposed to explain formation of the Himalayan-Tibetan orogenic system, including its high elevation and the mechanisms responsible for exhumation of its high-grade metamorphic rocks [e.g., England and Houseman, 1986, 1988; Harrison *et al.*, 1992; Clark and Royden, 2000; Tapponnier *et al.*, 2001]. However, although these geodynamic and tectonics models differ in timing and style, all consider that the orogen has remained in a convergent tectonic setting since initiation of collision between India and Eurasia at ~50 Ma. In the following we evaluate competing models proposed for exhumation of the HCC and activation of the STD in the light of our evidence that meteoric fluids penetrated the upper crust to depths beneath the brittle-ductile transition zone and reached the plastically deforming STD footwall (Figure 5d).

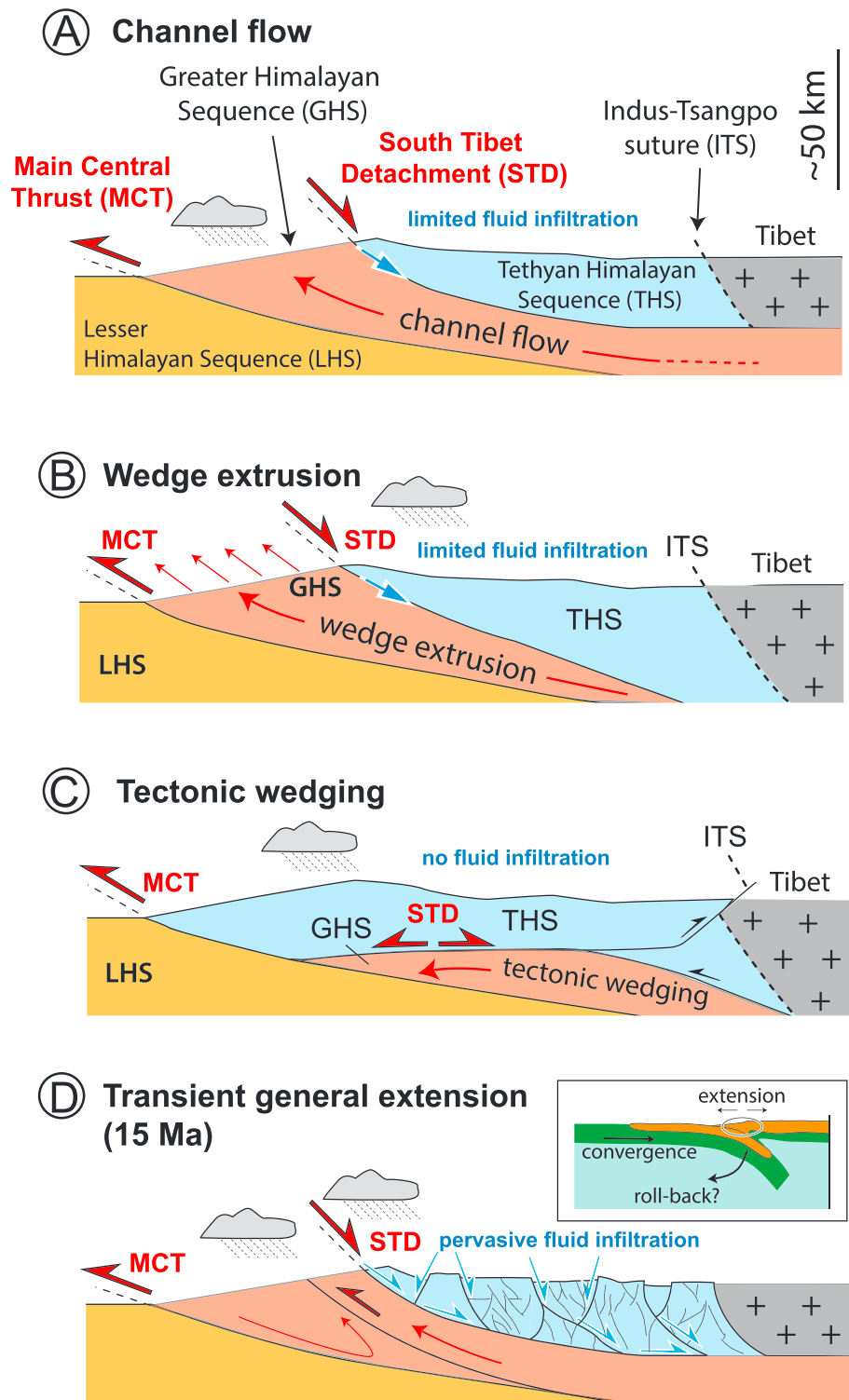


Figure 5. Models for exhumation of the Himalayan crystalline core. Models include (a) channel flow [Nelson *et al.*, 1996; Beaumont *et al.*, 2001; Hodges *et al.*, 2001], (b) wedge extrusion [Burchfiel and Royden, 1985; Grujic *et al.*, 1996; Grasemann *et al.*, 1999], and (c) tectonic wedging [Yin, 2006; Webb *et al.*, 2007]. (d) Conceptual model (from this study) proposing extensional tectonics in the upper Tethyan Himalayan plate (hanging wall to the STD) with development of E-W striking normal faults within a convergent setting (see text for explanation).

The channel flow [Nelson *et al.*, 1996; Beaumont *et al.*, 2001; Hodges *et al.*, 2001] and wedge extrusion [Burchfiel and Royden, 1985; Grujic *et al.*, 1996] models favor the southward extrusion of middle to lower crust as a result of overthickening of partially molten crust located to the north (Figures 5a and 5b). Here extrusion is accommodated by reverse- and normal-sense shearing on the MCT and STD at the base and top of the extruding tectonic unit, respectively. In this scenario the STD may have been active up to (or close to) the Earth's surface and could be infiltrated by meteoric fluids. In both models, the presence of steep normal faults in the hanging wall to the STD would increase fluid circulation. In the tectonic wedging model [Yin, 2006; Webb *et al.*, 2007] that involves the MCT and STD merging in their updip direction (Figure 5c), development of the STD is a consequence of early crustal thickening and development of duplex systems via underplating due to material being accreted from the down-going Indian crust. In this context, where the contact between the high-grade metamorphic rocks and the overlying Tethyan sedimentary units (marking the STD) remains at depth, it appears very unlikely that surface-derived fluids would be able to penetrate the crust down to the STD. In addition, the presence of steep normal faults might not extend to the horizontal segment of the STD. Although bending of the upper crust in response to movement on ramps might create fractures that could provide fluid pathways, the overall ability for fluids to penetrate down to the STDs along fractures would be less without steep normal faults. In contrast, fluid infiltration down to the STD footwall would be maximized if the Tethyan Himalayan sequence was subject to normal faulting (Figure 5d). Development of normal faulting in the Tethyan Himalayan sequence implies that the upper crust experienced stretching/extension. While remaining in a convergent setting, two scenarios triggering extension in the Tethyan sedimentary sequence overlying the STD may be considered: (1) gravitational instability and/or (2) Indian plate rollback.

1. As suggested for southern Tibet [Burg *et al.*, 1984; Burchfiel and Royden, 1985; Avouac, 2015], a change to positive elevation may have triggered gravitational spreading of the upper to middle crust in response to a vertical stress component. It is well recognized that local stress fields in the upper crust vary with topography [e.g., Bollinger *et al.*, 2004], and in our case study, it has been demonstrated that the Mount Everest region was standing at high elevation (≥ 5000 m) during the middle Miocene [Gébelin *et al.*, 2013]. As a consequence of crustal overthickening, the maximum principal compressive stress (1σ) in the upper part of the crust may have rotated from a north-south horizontal direction to a near vertical orientation, triggering the development of E-W striking normal faults within a tectonic regime still involving regional/crustal-scale north-south convergence [Burchfiel and Royden, 1985; Bollinger *et al.*, 2004]. Following the end of activity on the STD, this continued topographic load was expressed by E-W extension along the Himalayan arc from the late Miocene to the present.
2. North-south lithosphere-scale extension beneath the Tibetan Plateau may explain the rapid subsidence of the Kailas basin in southern Tibet from 26 to 21 Ma or later by southward rollback of Indian lithosphere [DeCelles *et al.*, 2011; Carrapa *et al.*, 2014]. This scenario involves southward retreat of the India-Asia suture and back-arc extension with development of tilted fault blocks in the upper plate.

Our results suggesting that E-W striking brittle normal faults affected the crust down to the brittle-ductile transition would support the idea of localized stretching/extension of the upper and middle crust in middle Miocene times (Figure 5d). However, a number of interconnected events occurring in late-early to middle Miocene times point to more complex larger-scale extensional tectonic processes that may have been in operation at that time: (1) deposition of the Kailas Formation during the early Miocene in a transtensional rift along the India-Asia suture zone [DeCelles *et al.*, 2011], (2) rapid exhumation of granulitized eclogites in NW Bhutan [Grujic *et al.*, 2011] and the Ama Drime Massif to the NE of Mount Everest [Cottle *et al.*, 2009; Kali *et al.*, 2010], and (3) eruption of mantle-derived potassic basalt lava flows in southern Tibet [e.g., Turner *et al.*, 1996].

Our results suggest that major geodynamic changes may have characterized the Mount Everest region during the middle Miocene from N-S stretching with development of E-W striking normal faults to orogen-parallel E-W extension as evidenced by N-S striking normal faults. Both types of normal faults may have served as conduits for fluids that, as observed for modern fluids issuing out of springs on N-S striking normal faults in the northern part of the Mount Everest region and the STDs near Nyalam, have penetrated down to shallow, intermediate, and even deep crustal levels [Newell *et al.*, 2008]. The present-day seismic activity observed in southern Tibet along active normal faults [e.g., Bollinger *et al.*, 2004; Avouac, 2015] suggests that the vertical stress field has not changed significantly over the last 15 Myr, as also suggested by stable isotope

paleoaltimetry [Gébelin *et al.*, 2013], indicating that the mean elevation of the central Himalaya at the longitude of Mount Everest (~5200 m) has remained stable since the middle Miocene.

7. Conclusion

Synkinematic biotite collected systematically over 200 m of structural section from the STD into the underlying mylonitic footwall exposed in the Rongbuk Valley reveals consistent middle Miocene $^{40}\text{Ar}/^{39}\text{Ar}$ plateau ages. The same mineral grains are interpreted to have exchanged isotopically at high temperature with D-depleted water ($\delta\text{D}_{\text{water}} = -150 \pm 5\text{‰}$) that originated as high-elevation meteoric water and infiltrated the crustal hydrologic system most likely during ductile extensional deformation. As observed for metamorphic core complexes of the North American Cordillera, we suggest that fluid flow in the STD footwall was intimately coupled to the porosity-permeability structure of the brittle upper Tethyan Himalayan sequence that was undergoing extension during the middle Miocene. This extensional event may have developed as a result of rotation of the maximum principle stress direction from horizontal north-south to near vertical, owing to the development of a topographic high in the Mount Everest region at ~15 Ma. Steep normal faults mapped in the Tethyan units above the detachment may represent a part of the conduit system that delivered surface-derived fluids down to the brittle-ductile transition while deformation in the STD footwall was active.

The STD can be traced for a distance of > 1500 km along the length of the Himalaya and is one of the fundamental structures within the Himalayan orogenic belt. The presence of surface-derived fluids in the STD footwall between 16.7 and 14.9 Ma, at least in the Mount Everest region, highlights the importance of the STD as a fault-controlled hydrothermal system sustained by the combination of heat advection (including leucogranite bodies; Hodges *et al.* [1998], Murphy and Harrison [1999], and Searle *et al.* [2003]) and the presence of a hydraulic head [Person *et al.*, 2007] generated by high topography in the region [Gébelin *et al.*, 2013].

Acknowledgments

A.M. and A.G. acknowledge funding through the LOEWE (Landes-Offensive zur Entwicklung Wissenschaftlich-ökonomischer Exzellenz) program of the State of Hesse (Germany) Ministry of Higher Education, Research, and the Arts. We thank J. Fiebig (Frankfurt) for laboratory support. R.D.L. and M.J. gratefully acknowledge funding from NSF grant EAR 0207524 to R.D.L. and M. Searle (Oxford University) that supported their microstructural and quartz crystal fabric/deformation thermometry work in the Rongbuk Valley. C.T. gratefully acknowledges support from NSF grant EAR 0838541. Rock samples described in this paper were collected by M.J., J. Cottle (UC Santa Barbara), and D. Newell (Utah State University) during fieldwork in 2005 and 2007. L. Duncan assisted in 2007. Support for sample collection was provided by a 2010 Fellowship from the Virginia Tech College of Science (Jessup), a National Science Foundation Integrative Graduate Education and Research Traineeship (Newell), University of New Mexico research grants (Newell), and a New Zealand Tertiary Education Commission Doctoral Scholarship (Cottle). Any use of trade, product, or firm names is for descriptive purposes only and does not imply endorsement by the U.S. Government. We acknowledge the very insightful and careful remarks of R. Thiede, S. Johnstone, an anonymous reviewer, and Editor C. Faccenna, which clarified and improved the manuscript.

References

- Avouac, J.-P. (2015), Mountain building: From earthquakes to geologic deformation, in *Treatise on Geophysics*, 2nd ed., vol. 6, edited by G. Schubert, pp. 381–432, Elsevier, Amsterdam.
- Beaumont, C., R. A. Jamieson, M. H. Nguyen, and B. Lee (2001), Himalayan tectonics explained by extrusion of a low-viscosity crustal channel coupled to focused surface denudation, *Nature*, *414*, 738–742, doi:10.1038/414738a.
- Beaumont, C., R. A. Jamieson, M. H. Nguyen, and S. Medvedev (2004), Crustal channel flows: 1. Numerical models with applications to the tectonics of the Himalayan–Tibetan orogen, *J. Geophys. Res.*, *109*, B06406, doi:10.1029/2003JB002809.
- Bollinger, L., J. P. Avouac, R. Cattin, and M. R. Pandey (2004), Stress building in the Himalaya, *J. Geophys. Res.*, B11405, doi:10.1029/2003JB002911.
- Burchfiel, B. C., and L. H. Royden (1985), North–south extension within the convergent Himalayan region, *Geology*, *13*, 679–682.
- Burchfiel, B. C., Z. Chen, K. V. Hodges, Y. Liu, L. H. Royden, C. Deng, and J. Xu (1992), The south Tibet detachment system, Himalayan orogen: Extension contemporaneous with and parallel to shortening in a collisional mountain belt, *Geol. Soc. Am. Bull. Spec. Pap.*, *269*, 1–41.
- Burg, J. P., M. Brunel, D. Gapais, G. M. Chen, and G. H. Liu (1984), Deformation of leucogranites of the crystalline main central sheet in southern Tibet (China), *J. Struct. Geol.*, *6*, 535–542.
- Campani, M., A. Mulch, O. Kempf, F. Schlunegger, and N. Mancktelow (2012), Miocene paleotopography of the Central Alps, *Earth Planet. Sci. Lett.*, *337*–*338*, 174–185.
- Carosi, R., B. Lombardo, G. Molli, G. Musumeci, and P. C. Pertusati (1998), The South Tibetan Detachment system in the Rongbuk valley, Everest region. Deformation features and geological implications, *J. Asian Earth Sci.*, *16*, 299–311.
- Carosi, R., B. Lombardo, G. Musumeci, and P. C. Pertusati (1999), Geology of the Higher Himalayan crystallines in KhumbuHimal (eastern Nepal), *J. Asian Earth Sci.*, *17*, 785–803.
- Carosi, R., C. Montomoli, D. Rubatto, and D. Visonà (2013), Leucogranite intruding the South Tibetan Detachment in western Nepal: Implications for exhumation models in the Himalayas, *Terra Nova*, *25*, 478–489.
- Carrapa, B., D. A. Orme, P. G. DeCelles, P. Kapp, M. A. Cosca, and R. Waldrip (2014), Miocene burial and exhumation of the India-Asia collision zone in southern Tibet: Response to slab dynamics and erosion, *Geology*, *42*, 443–446.
- Carrapa, B., X. Robert, P. G. DeCelles, D. A. Orme, S. N. Thomson, and L. M. Schoenbohm (2016), Asymmetric exhumation of the Mount Everest region: Implications for the tectono-topographic evolution of the Himalaya, *Geology*, *44*, 611–614, doi:10.1130/G37756.1.
- Chambers, J., R. Parrish, T. Argles, N. Harris, and M. Horstwood (2011), A short duration pulse of ductile normal shear on the outer South Tibetan Detachment in Bhutan: Alternating channel flow and critical taper mechanics of the eastern Himalaya, *Tectonics*, *30*, TC2005, doi:10.1029/2010TC002784.
- Chemenda, A. I., J. P. Burg, and M. Mattauer (2000), Evolutionary model of the Himalaya-Tibet system: Geopem based on new modeling, geological and geophysical data, *Earth Planet. Sci. Lett.*, *174*, 397–409.
- Chi-Hsiang, Y., and K. Shih-Tseng (1978), Stratigraphy of the Mont JolmoLungma and its north slope, *Sci. Sin.*, *5*, 629–644.
- Clark, M. K., and L. H. Royden (2000), Topographic ooze: Building the eastern margin of Tibet by lower crustal flow, *Geology*, *28*, 703–706.
- Coplen, T. B., et al. (2002), Compilation of minimum and maximum isotope ratios of selected elements in naturally occurring terrestrial materials and reagents, *U.S. Geol. Surv. Water-Resources Investigation Rep.*, *01-4222*, 98 pp.
- Corthouts, T. L., D. R. Lageson, and C. A. Shaw (2015), Polyphase deformation, dynamic metamorphism, and metasomatism of Mount Everest's summit limestone, east central Himalaya, Nepal/Tibet, *Lithosphere*, *8*, 38–57, doi:10.1130/L473.1.

- Cottle, J. M., M. J. Jessup, D. L. Newell, M. S. A. Horstwood, S. R. Noble, R. R. Parrish, D. J. Waters, and M. P. Searle (2009), Geochronology of granulitized eclogite and associated rocks from the AmaDrime Massif: Implications for the tectonic evolution of the south Tibetan Himalaya, *Tectonics*, *28*, TC1002, doi:10.1029/2008TC002256.
- Cottle, J. M., M. P. Searle, M. J. Jessup, J. L. Crowley, and R. D. Law (2015), Rongbuk re-visited: Geochronology of leucogranites in the footwall of the South Tibetan Detachment system, Everest region, southern Tibet, *Lithos*, *227*, 94–106, doi:10.1016/j.lithos.2015.03.019.
- Dalrymple, G. B., E. C. Alexander, M. A. Lanphere, and G. P. Kraker (1981), Irradiation of samples for $^{40}\text{Ar}/^{39}\text{Ar}$ dating using the geological survey TRIGA reactor, *U.S. Geol. Surv. Prof. Pap.*, *1176*, 55 pp., Reston, Va.
- Daniel, C. G., L. S. Hollister, R. R. Parrish, and D. Grujic (2003), Exhumation of the Main Central Thrust from lower crustal depths, eastern Bhutan Himalaya, *J. Metamorph. Geol.*, *21*, 317–334.
- DeCelles, P., P. Kapp, J. Quade, and G. Gehrels (2011), Oligocene-Miocene Kailas basin, south-western Tibet: Record of postcollisional upper-plate extension in the Indus-Yarlung suture zone, *Geol. Soc. Am. Bull.*, *123*, 1337–1362, doi:10.1130/B30258.1.
- Ding, L., et al. (2017), Quantifying the rise of the Himalaya orogeny and implications for the South Asian monsoon, *Geology*, doi:10.1130/G38583.1.
- Dunlap, W. J. (1992), Structure, kinematics, and cooling history of the Airtunga Nappe complex, central Australia, PhD thesis, Univ. of Minnesota, Minn.
- Edwards, M. A., W. S. F. Kidd, J. Li, Y. Yue, and M. Clark (1996), Multi-stage development of the southern Tibet detachment system near Khulakangri. New data from Gonto La, *Tectonophysics*, *260*, 1–19, doi:10.1016/0040-1951(96)00073-X.
- Edwards, M. A., A. Pecher, W. S. F. Kidd, B. C. Burchfiel, and L. H. Royden (1999), Southern Tibet detachment system at Khulakangri, eastern Himalaya: A large-area, shallow detachment stretching into Bhutan?, *J. Geol.*, *107*, 623–631, doi:10.1086/314366.
- England, P. C., and G. A. Houseman (1986), Finite strain calculations of continental deformation: 2. Comparison with the India-Asia collision, *J. Geophys. Res.*, *91*, 3664–3676, doi:10.1029/JB091iB03p03664.
- England, P. C., and G. A. Houseman (1988), The mechanics of the Tibetan Plateau, *Philos. Trans. R. Soc. London, Ser. A*, *326*, 301–320.
- Faleiros, F. M., R. Moraes, M. Pavan, and G. A. C. Campanha (2016), A new empirical calibration of the quartz *c*-axis fabric opening-angle deformation thermometer, *Tectonophysics*, *671*, 173–182, doi:10.1016/j.tecto.2016.01.014.
- Field, C. W., and R. H. Fife (1985), Light stable-isotope systematics in the epithermal environment, in *Geology and Geochemistry of Epithermal Systems*, *Rev. Econ. Geol.*, vol. 2, edited by B. R. Berger and P. M. Bethke, pp. 99–128, Soc. of Econ. Geol., Boulder, Colo.
- Fontes, J. C., and R. Gonfiantini (1967), Comportement isotopique au cours de l'évaporation de deux bassins Sahariens, *Earth Planet. Sci. Lett.*, *3*, 258–266.
- Fricke, H. C., S. M. Wickham, and J. R. O'Neil (1992), Oxygen and hydrogen isotope evidence for meteoric water infiltration during mylonitization and uplift in the Ruby Mountains-East Humboldt Range core complex, Nevada, *Contrib. Mineral. Petrol.*, *111*, 203–221.
- Gébelin, A., A. Mulch, C. Teyssier, M. Heizler, T. Vennemann, and N. C. A. Seaton (2011), Oligo-Miocene extensional tectonics and fluid flow across the Northern Snake Range detachment system, Nevada, *Tectonics*, *30*, TC5010, doi:10.1029/2010TC002797.
- Gébelin, A., A. Mulch, C. Teyssier, C. P. Chamberlain, and M. Heizler (2012), Coupled basin-detachment systems as paleoaltimetry archives of the western North American Cordillera, *Earth Planet. Sci. Lett.*, *335–336*, 36–47, doi:10.1016/j.epsl.2012.04.029.
- Gébelin, A., A. Mulch, C. Teyssier, M. J. Jessup, R. D. Law, and M. Brunel (2013), The Miocene elevation of Mount Everest, *Geology*, *41*, 799–802, doi:10.1130/G34331.1.
- Gébelin, A., C. Teyssier, M. T. Heizler, and A. Mulch (2015), Meteoric water circulation in a rolling-hinge detachment system (northern Snake Range core complex, Nevada), *Geol. Soc. Am. Bull.*, *127*, 149–161, doi:10.1130/B31063.1.
- Godin, L., D. Grujic, R. D. Law, and M. P. Searle (2006), Channel flow, ductile extrusion and exhumation in continental collision zones: An introduction, *Geol. Soc. London, Spec. Publ.*, *268*, 1–23.
- Gong, B., Y. F. Zheng, and R. X. Chen (2007), TC/EA-MS online determination of hydrogen isotope composition and water concentration in eclogitic garnet, *Phys. Chem. Miner.*, *34*, 687–698.
- Gottardi, R., C. Teyssier, A. Mulch, T. W. Vennemann, and M. L. Wells (2011), Preservation of extreme transient geotherm in the Raft River detachment shear zone, *Geology*, *39*(8), 759–762.
- Grasemann, B., H. Fritz, and J.-C. Vannay (1999), Quantitative kinematic flow analysis from the Main Central Thrust zone (NW-Himalaya, India): Implications for a decelerating strain path and the extrusion of orogenic wedges, *J. Struct. Geol.*, *21*, 837–853.
- Grujic, D., M. Casey, C. Davidson, L. S. Hollister, R. Kundig, T. Pavlis, and S. Schmid (1996), Ductile extrusion of the Higher Himalayan crystalline in Bhutan: Evidence from quartz microfibrils, *Tectonophysics*, *260*, 21–43.
- Grujic, D., L. S. Hollister, and R. R. Parrish (2002), Himalayan metamorphic sequence as an orogenic channel: Insight from Bhutan, *Earth Planet. Sci. Lett.*, *198*, 177–191.
- Grujic, D., C. J. Warren, and J. L. Wooden (2011), Rapid synconvergent exhumation of Miocene aged lower orogenic crust in the eastern Himalaya, *Lithosphere*, *3*, 346–366, doi:10.1130/L154.1.
- Hames, W. E., and S. A. Bowring (1994), An empirical evaluation of the argon diffusion geometry in muscovite, *Earth Planet. Sci. Lett.*, *124*, 161–169.
- Harrison, T. M. (1981), Diffusion of ^{40}Ar in hornblende, *Contrib. Mineral. Petrol.*, *78*, 324–331.
- Harrison, T. M., and J. D. Fitz Gerald (1986), Exsolution in hornblende and its consequences for $^{40}\text{Ar}/^{39}\text{Ar}$ age spectra and closure temperature, *Geochim. Cosmochim. Acta*, *50*, 247–253.
- Harrison, T. M., I. Duncan, and I. McDougall (1985), Diffusion of ^{40}Ar in biotite: Temperature, pressure and compositional effects, *Geochim. Cosmochim. Acta*, *49*, 2461–2468.
- Harrison, T. M., P. Copeland, W. S. F. Kidd, and A. Yin (1992), Raising Tibet, *Science*, *255*, 1663–1670.
- Harrison, T. M., J. Célérier, A. B. Aikman, J. Hermann, and M. T. Heizler (2009), Diffusion of ^{40}Ar in muscovite, *Geochim. Cosmochim. Acta*, *73*, 1039–1051.
- Heim, A., and A. Gansser (1939), Central Himalaya, in *Geological Observations of Swiss*, pp. 1–246, Gebrüder Fretz, 1939. Hindustan Publ. Corp., Delhi.
- Hetzl, R., H. Zwingmann, A. Mulch, K. Gessner, C. Akal, A. Hampel, T. Güngör, R. Petschick, T. Mikes, and F. Wedin (2013), K-Ar ages and hydrogen isotope data from detachment fault systems in the Menderes Massif (Turkey): Implications for the timing of brittle deformation and fluid flow, *Tectonics*, *32*, 1–13, doi:10.1002/tect.20031.
- Hirth, G., and J. Tullis (1992), Dislocation creep regimes in quartz aggregates, *J. Struct. Geol.*, *14*, 145–159.
- Hodges, K. V., R. R. Parrish, T. B. Housh, D. R. Lux, B. C. Burchfiel, L. H. Royden, and Z. Chen (1992), Simultaneous Miocene extension and shortening in the Himalayan orogen, *Science*, *258*, 1446–1470.
- Hodges, K. V., R. R. Parrish, and M. P. Searle (1996), Tectonic evolution of the central Annapurna Range, Nepalese Himalayas, *Tectonics*, *15*, 1264–1291, doi:10.1029/96TC01791.

- Hodges, K. V., S. Bowring, K. Davidek, D. Hawkins, and M. Krol (1998), Evidence for rapid displacement on Himalayan normal faults and the importance of tectonic denudation in the evolution of mountain ranges, *Geology*, *26*, 483–486.
- Hodges, K. V., J. M. Hurtado, and K. X. Whipple (2001), Southward extrusion of Tibetan crust and its effect on Himalayan tectonics, *Tectonics*, *20*, 799–809, doi:10.1029/2001TC001281.
- Hoefs, J. (2004), *Stable Isotope Geochemistry*, 5th ed., pp. 239, Springer, Berlin, Heidelberg, New York.
- Holk, G. J., and H. P. Taylor (2007), $^{18}\text{O}/^{16}\text{O}$ evidence for contrasting hydrothermal regimes involving magmatic and meteoric-hydrothermal waters in the Valhalla metamorphic core complex, British Columbia, *Econ. Geol.*, *102*, 1063–1078.
- Jessel, M. W. (1987), Grain-boundary migration microstructures in a naturally deformed quartzite, *J. Struct. Geol.*, *9*, 1007–1014.
- Jessup, M. J., and J. M. Cottle (2010), Progression from south-directed extrusion to orogen-parallel extension in the southern margin of the Tibetan Plateau, Mount Everest region, Tibet, *J. Geol.*, *118*, 467–486.
- Jessup, M. J., R. D. Law, M. P. Searle, and M. S. Hubbard (2006), Structural evolution and vorticity of flow during extrusion and exhumation of the Greater Himalayan Slab, Mount Everest massif, Tibet/Nepal: Implications for orogeny-scale flow partitioning, in *Channel Flow, Extrusion, and Exhumation in Continental Collision Zones*, *Geol. Soc. Spec. Publ.*, vol. 268, edited by R. D. Law, M. P. Searle, and L. Godin, pp. 379–414.
- Jessup, M. J., J. M. Cottle, M. P. Searle, R. D. Law, R. J. Tracy, D. L. Newell, and D. J. Waters (2008), *P-T-t-D* paths of Everest Series schist, *J. Metamorph. Geol.*, *26*, 717–739.
- Jouzel, J., C. Lorius, J. R. Petit, C. Genthon, N. I. Barkov, V. M. Kotlyakov, and V. M. Petrov (1987), Vostok ice core: A continuous isotope temperature record over the last climatic cycle (160,000 years), *Nature*, *329*, 403–408.
- Kali, E., P. H. Leloup, N. Arnaud, G. Maheo, D. Liu, E. Boutonnet, J. Van der Woerd, X. Liu, J. Liu-Zeng, and H. Li (2010), Exhumation history of the deepest central Himalayan rocks, AmaDrime range: Key pressure-temperature-deformation-time constraints on orogenic models, *Tectonics*, *29*, TC2014, doi:10.1029/2009TC002551.
- Kellett, D. A., and D. Grujic (2012), New insight into the South Tibetan Detachment system: Not a single progressive deformation, *Tectonics*, *31*, TC2007, doi:10.1029/2011TC002957.
- Kellett, D. A., D. Grujic, and S. Erdmann (2009), Miocene structural reorganization of the South Tibetan Detachment, eastern Himalaya: Implications for continental collision, *Lithosphere*, *1*, 259–281.
- Kellett, D. A., D. Grujic, C. Warren, J. Cottle, R. Jamieson, and T. Tenzin (2010), Metamorphic history of a syn-convergent orogeny-parallel detachment: The South Tibetan Detachment system, Bhutan Himalaya, *J. Metamorph. Geol.*, *28*, 785–808, doi:10.1111/j.1525-1314.2010.00893.x.
- Kellett, D. A., D. Grujic, I. Coutand, J. Cottle, and M. Mukul (2013), The South Tibetan Detachment system facilitates ultra rapid cooling of granulite-facies rocks in Sikkim Himalaya, *Tectonics*, *32*, 252–270, doi:10.1002/tect.20014.
- Kuiper, K. F., A. Deino, F. J. Hilgen, W. Krijgsman, P. R. Renne, and J. R. Wijbrans (2008), Synchronizing rock clocks of Earth history, *Science*, *320*, 500–504.
- Law, R. D. (2014), Deformation thermometry based on quartz *c*-axis fabrics and recrystallization microstructures: A review, *J. Struct. Geol.*, *66*, 129–161.
- Law, R. D., M. P. Searle, and R. L. Simpson (2004), Strain, deformation temperatures and vorticity of flow at the top of the Greater Himalayan Slab, Everest massif, Tibet, *J. Geol. Soc. London*, *161*, 305–320.
- Law, R. D., M. J. Jessup, M. P. Searle, M. K. Francis, D. J. Waters, and J. M. Cottle (2011), Telescoping of isotherms beneath the South Tibetan Detachment system, Mount Everest massif, *J. Struct. Geol.*, *33*, 1569–1594, doi:10.1016/j.jsg.2014.05.023.
- Lee, J., C. Hager, S. R. Wallis, D. F. Stockli, M. J. Whitehouse, M. Aoya, and Y. Wang (2011), Middle to late Miocene extremely rapid exhumation and thermal reequilibration in the Kung Co rift, southern Tibet, *Tectonics*, *30*, TC2007, doi:10.1029/2010TC002745.
- Lee, J.-Y., K. Marti, J. P. Severinghaus, K. Kawamura, H. S. Yoo, J. B. Lee, and J. S. Kim (2006), A redetermination of the isotopic abundances of atmospheric Ar, *Geochim. Cosmochim. Acta*, *70*, 4507–4512.
- Lefort, P. (1975), Himalayas, the collided range: Present knowledge of continental arc, *Am. J. Sci.*, *A*, *275*, 1–44.
- Leloup, P. H., G. Maheo, N. Arnaud, E. Kali, E. Boutonnet, D. Liu, X. Liu, and H. Li (2010), The south Tibet detachment shear zone in the Dinggye area: Time constraints on extrusion models of the Himalayas, *Earth Planet. Sci. Lett.*, *292*, 1–16, doi:10.1016/j.epsl.2009.12.035.
- Lombardo, B., P. Pertusati, and S. Borgi (1993), Geology and tectonomagmatic evolution of the eastern Himalaya along the Chomolungma-Makalu transect, in *Himalayan Tectonics*, *Geol. Soc. Spec. Publ.*, vol. 74, edited by P. J. Treloar and M. P. Searle, pp. 341–355.
- Losh, S. (1997), Stable isotope and modeling studies of fluid-rock interaction associated with the Snake Range and Mormon Peak detachment faults, Nevada, *Geol. Soc. Am. Bull.*, *109*, 300–323.
- Mertanen, S., and F. Karell (2012), Palaeomagnetic and AMS studies on Satulinmaki and Kojjarvi fault and shear zones, in *Gold in southern Finland: Results of GTK studies 1998–2011*, *Spec. Pap.*, vol. 52, edited by S. Gronholm and N. Karkkainen, pp. 195–226, Geol. Surv. of Finland, Espoo.
- Methner, K., A. Mulch, C. Teyssier, M. Wells, M. Cosca, R. Gottardi, A. Gébelin, and C. P. Chamberlain (2015), Eocene and Miocene extension, meteoric fluid infiltration and core complex formation in the Great Basin (Raft River Mountains, Utah), *Tectonics*, *34*, 1–14, doi:10.1002/2014TC003766.
- Min, K., R. Mundil, P. R. Renne, and K. R. Ludwig (2000), A test for systematic errors in $^{40}\text{Ar}/^{39}\text{Ar}$ geochronology through comparison with U/Pb analysis of a 1.1-Ga rhyolite, *Geochim. Cosmochim. Acta*, *64*, 73–98.
- Mulch, A., C. Teyssier, M. A. Cosca, O. Vanderhaeghe, and T. Vennemann (2004), Reconstructing paleoelevation in eroded orogens, *Geology*, *32*, 525–528.
- Mulch, A., M. A. Cosca, J. Fiebig, and A. Andresen (2005), Time scales of mylonitic deformation and meteoric fluid infiltration during extensional detachment faulting: An integrated in situ $^{40}\text{Ar}/^{39}\text{Ar}$ geochronology and stable isotope study of the Porsgrunn-Kristiansand shear zone (Southern Norway), *Earth Planet. Sci. Lett.*, *233*, 375–390.
- Mulch, A., C. Teyssier, M. A. Cosca, and T. Vennemann (2006), Thermomechanical analysis of strain localization in a detachment zone, *J. Geophys. Res.*, *111*, B12405, doi:10.1029/2005JB004032.
- Murphy, M. A., and T. M. Harrison (1999), Relationship between leucogranites and the Qomolangma detachment in the Rongbuk valley, south Tibet, *Geology*, *27*, 831–834.
- Nagy, C., L. Godin, B. Antolin, J. Cottle, and D. Archibald (2015), Mid-Miocene initiation of orogen-parallel extension, NW Nepal Himalaya, *Lithosphere*, *7*, 483–502.
- Nelson, K. D., et al. (1996), Partially molten middle crust beneath southern Tibet: Synthesis of project INDEPTH results, *Science*, *274*, 1684–1696.
- Nesbitt, B. E., and K. Muehlenbachs (1995), Geochemistry of syntectonic, crustal fluid regimes along the Lithoprobe southern Canadian Cordillera transect, *Can. J. Earth Sci.*, *32*, 1699–1719.

- Newell, D. L., M. J. Jessup, J. M. Cottle, D. R. Hilton, Z. D. Sharp, and T. P. Fischer (2008), Aqueous and isotope geochemistry of mineral springs along the southern margin of the Tibetan Plateau: Implications for fluid sources and regional degassing of CO₂, *Geochem. Geophys. Geosyst.*, *9*, Q08014, doi:10.1029/2008GC002021.
- Paterson, M. S. (1995), A theory for granular flow accommodated by material transfer via an intergranular fluid, *Tectonophysics*, *245*, 135–152.
- Pécher, A. (1989), The metamorphism in the central Himalaya, *J. Metamorph. Geol.*, *7*, 31–41.
- Person, M., A. Mulch, C. Teyssier, and Y. Gao (2007), Isotope transport and exchange within metamorphic core complexes, *Am. J. Sci.*, *307*, 555–589.
- Poage, M. A., and C. P. Chamberlain (2001), Empirical relationships between elevation and the stable isotope composition of precipitation and surface waters: Considerations for studies of paleoelevation change, *Am. J. Sci.*, *301*, 1–15, doi:10.2475/ajs.301.1.1.
- Pognante, U., and P. Benna (1993), Metamorphic zonation, migmatization and leucogranites along the Everest transect of eastern Nepal and Tibet: Record of an exhumation history, in *Himalayan Tectonics, Geol. Soc. Spec. Publ.*, vol. 74, edited by P. J. Treloar and M. P. Searle, pp. 323–340.
- Polyea, R. M., E. W. Van Dusen, and M. P. Fisher (2015), Topographically driven fluid flow within orogenic wedges: Effects of taper angle and depth-dependent permeability, *Geosphere*, *11*, 1427–1437.
- Quilichini, A., L. Siebenaller, W. O. Nachlas, C. Teyssier, T. W. Vennemann, M. T. Heizler, and A. Mulch (2015), Infiltration of meteoric fluids in an extensional detachment shear zone (Kettle dome, WA, USA): How quartz dynamic recrystallization relates to fluid-rock interaction, *J. Struct. Geol.*, *71*, 71–85.
- Quilichini, A., L. Siebenaller, C. Teyssier, and T. Vennemann (2016), Magmatic and meteoric fluid flow in the Bitterroot extensional detachment shear zone (MT, USA) from ductile to brittle conditions, *J. Geodyn.*, doi:10.1016/j.jog.2016.05.006.
- Renard, F., D. Dysthe, J. Feder, K. Bjørlykke, and B. Jamtveit (2001), Enhanced pressure solution creep rates induced by clay particles: Experimental evidence in salt aggregates, *Geophys. Res. Lett.*, *28*, 1295–1298, doi:10.1029/2000GL012394.
- Ring, U., and J. Glodny (2010), No need for lithospheric extension for exhuming UHP rocks by normal faulting, *J. Geol. Soc.*, *167*, 225–228, doi:10.1144/0016-76492009-134.
- Rutter, E. H., and D. H. Mainprice (1979), On the possibility of slow fault slip controlled by a diffusive mass transfer process, *Gerlands Beitr. Geophys.*, *88*, 154–162.
- Sakai, H., M. Sawada, Y. Takigami, Y. Orihashi, T. Danhara, H. Iwano, Y. Kuwahara, Q. Dong, H. Cai, and J. Li (2005), Geology of the summit limestone of Mount Qomolangma (Everest) and cooling history of the Yellow Band under the Qomolangma detachment, *Isl. Arc*, *14*, 297–310.
- Saxena, A., H. K. Sachan, P. K. Mukherjee, and D. K. Mukhopaddhya (2012), Fluid-rock interaction across the South Tibetan Detachment, Garhwal Himalaya (India): Mineralogical and geochemical evidences, *J. Earth. Syst. Sci.*, *121*, 29–44.
- Schultz, M., K. V. Hodges, T. A. Ehlers, M. Van Soest, and J. A. Wartho (2017), Thermochronologic constraints on the slip history of the South Tibetan Detachment system in the Everest region, southern Tibet, *Earth Planet. Sci. Lett.*, *459*, 105–117, doi:10.1016/j.epsl.2016.11.022.
- Searle, M. P. (2003), Geological map of the Mount Everest region, Nepal and south Tibet, Scale 1:100,000, Department of Earth Sciences, Oxford Univ., U. K.
- Searle, M. P., R. L. Simpson, R. D. Law, D. J. Watersand, and R. R. Parrish (2002), Quantifying displacement on the South Tibetan Detachment normal fault, Everest massif, and the timing of crustal thickening and uplift in the Himalaya and south Tibet, *J. Nepal Geol. Soc.*, *26*, 1–6.
- Searle, M. P., R. L. Simpson, R. D. Law, R. R. Parrish, and D. J. Waters (2003), The structural geometry, metamorphic and magmatic evolution of the Everest massif, High Himalaya of Nepal–south Tibet, *J. Geol. Soc. London*, *160*, 345–366.
- Searle, M. P., R. D. Law, and M. J. Jessup (2006), Crustal structure, restoration and evolution of the Greater Himalaya: Implication for channel flow and ductile extrusion of the middle crust, in *Channel Flow, Extrusion and Exhumation in Continental Collision Zones, Geol. Soc. Spec. Publ.*, vol. 268, edited by R. L. Law, M. P. Searle, and L. Godin, pp. 355–378.
- Searle, M. P., R. D. Law, L. Godin, K. P. Larson, M. J. Streule, J. M. Cottle, and M. J. Jessup (2008), Defining the Himalayan Main Central Thrust in Nepal, *J. Geol. Soc. London*, *165*, 523–534.
- Searle, M. P., J. M. Cottle, M. J. Streule, and D. J. Waters (2010), Crustal melt granites and migmatites along the Himalaya: Melt source, segregation, transport and granite emplacement mechanisms, *Trans. R. Soc. Edinburgh*, *100*, 219–233, doi:10.1017/S175569100901617X.
- Sheppard, S. M. F. (1986), Characterization and isotopic variations in natural waters, *Rev. Mineral. Geochem.*, *16*, 165–184.
- Simpson, R. L., R. R. Parrish, M. P. Searle, and D. J. Waters (2000), Two episodes of monazite crystallization during metamorphism and crustal melting in the Everest region of the Nepalese Himalaya, *Geology*, *28*, 403–406.
- Spicer, R. A., B. B. W. Harris, M. Widdowson, A. B. Herman, S. Guo, P. J. Valdes, J. A. Wolfe, and S. P. Kelley (2003), Constant elevation of southern Tibet over the past 15 million years, *Nature*, *421*, 622–624, doi:10.1038/nature01356.
- Streule, M. J., A. Carter, M. P. Searle, and J. M. Cottle (2012), Constraints on brittle field exhumation of the Everest-Makalu section of the Greater Himalayan sequence: Implications for models of crustal flow, *Tectonics*, *31*, TC3010, doi:10.1029/2011TC003062.
- Suzuoki, T., and S. Epstein (1976), Hydrogen isotope fractionation between OH-bearing minerals and water, *Geochim. Cosmochim. Acta*, *40*, 1229–1240.
- Tapponnier, P., X. Zhiqin, F. Roger, B. Meyer, N. Arnaud, G. Wittlinger, and Y. Jinsui (2001), Oblique stepwise rise and growth of the Tibet Plateau, *Science*, *294*, 1671–1677.
- Taylor, H. P. (1990), Oxygen and hydrogen isotope constraints on the deep circulation of surface waters into zones of hydrothermal metamorphism and melting, in *The Role of Fluids in Crustal Processes*, edited by J. D. Bredehoeft and D. L. Morton, pp. 72–95, National Academy Press, Washington, D. C.
- Ten Grotenhuis, S. M., R. A. J. Trouw, and C. W. Passchier (2003), Evolution of mica fish in mylonitic rocks, *Tectonophysics*, *372*, 1–21.
- Turner, S., N. Arnaud, L. Liu, N. Rogers, C. Hawksworth, N. Harris, S. Kelley, P. Van Calstere, and W. M. Deng (1996), Post-collisional shoshonitic volcanism on the Tibetan Plateau: Implication for convective thinning of the lithosphere and the source of ocean island basalts, *J. Petrol.*, *37*, 45–71.
- Vannay, J. C., and B. Grasemann (2001), Himalayan inverted metamorphism and syn-convergence extension as a consequence of a general shear extrusion, *Geol. Mag.*, *138*, 253–276.
- Viskupic, K., K. V. Hodges, and S. A. Bowring (2005), Timescales of melt generation and the thermal evolution of the Himalayan metamorphic core, Everest region, eastern Nepal, *Contrib. Mineral. Petrol.*, *149*, 1–21, doi:10.1007/s00410-004-0628-5.
- Warr, L. N., and S. Cox (2001), Clay mineral transformations and weakening mechanisms along the Alpine Fault, New Zealand, in *The Nature and Tectonics Significance of Fault Zone Weakening, Geol. Soc. Spec. Publ.*, vol. 186, edited by R. E. Holdsworth et al., pp. 85–101.
- Waters, D. J., R. D. Law, and M. P. Searle (2006), Metamorphic evolution of the upper parts of the Greater Himalayan Slab, Mount Everest area, from the 1933 sample collection of L. R. Wager (abstract), *J. Asian Earth Sci.*, *26*, 168.

- Webb, A. A. G., A. Yin, T. M. Harrison, J. C  lerier, and W. P. Burgess (2007), The leading edge of the Greater Himalayan crystallines revealed in the NW Indian Himalaya: Implications for the evolution of the Himalayan orogen, *Geology*, *35*, 955–958, doi:10.1130/G23931A.1.
- Webb, A. A. G., A. Yin, T. M. Harrison, J. C  lerier, G. E. Gehrels, C. E. Manning, and M. Grove (2011), Cenozoic tectonic history of the Himachal Himalaya (northwestern India), and its constraints on the formation mechanism of the Himalayan orogen, *Geosphere*, *7*, 1013–1061, doi:10.1130/GES00627.1.
- Wernicke, B., and B. C. Burchfiel (1982), Modes of extensional tectonics, *J. Struct. Geol.*, *4*, 105–115.
- Whitney, D. L., C. Teyssier, P. Rey, and W. R. Buck (2013), Continental and oceanic core complexes, *Geol. Soc. Am. Bull.*, *125*, 273–298.
- Wintsch, R. P., R. Christofferson, and A. K. Kronenberg (1995), Fluid-rock reaction weakening of fault zones, *J. Geophys. Res.*, *100*, 13,021–13,032, doi:10.1029/94JB02622.
- Wu, C., et al. (1998), Yadong cross structure and South Tibetan Detachment in the east central Himalaya (89  –90  E), *Tectonics*, *17*, 28–45, doi:10.1029/97TC03386.
- Yin, A. (2006), Cenozoic tectonic evolution of the Himalayan orogen as constrained by along strike variation of structural geometry, exhumation history, and foreland sedimentation, *Earth Sci. Rev.*, *76*, 1–131, doi:10.1016/j.earscirev.2005.05.004.